Eddies drive meridionally asymmetric upwelling in the equatorial Pacific

Daniel B. Whitt,[a] Frank O. Bryan,[b] William Kessler,[c,d] LuAnne Thompson,[d] Anna-Lena Deppenmeier,[e]

[a] *NASA Ames Research Center, Moffett Field, CA, USA*

[b] *NSF National Center for Atmospheric Research, Boulder, CO, USA*

[c] *NOAA Pacific Marine Environmental Lab, Seattle, WA, USA*

[d] *University of Washington, Seattle, WA, USA*

[e] *University of Liverpool, Liverpool, UK*

Corresponding author: Daniel B. Whitt, daniel.b.whitt@nasa.gov

ABSTRACT: Climatological equatorial Pacific upwelling has been quantified observationally and reproduced in numerical simulations. However, the fine scale structure and the processes that drive it remain unclear. A 1/20°-resolution regional ocean simulation of the equatorial Pacific cold tongue encompassing 95°W to 170°W from 1999 through 2018 is used to investigate these physical processes. The simulated upwelling at 50 m is asymmetric across the equator and stronger to the north than to the south, consistent with simulated and observed meridional divergence at 15 m. A two-dimensional Eliassen model of the meridional circulation is formulated to investigate the linear response to disruptions of the dominant thermal wind balance. The linearity of the diagnostic model is then exploited to separate and quantify the circulation owing to eddy fluxes from the dominant wind-driven circulation. A tripolar eddy-driven circulation is found in the top 100 m with upwelling of 0.7 m/d on average near 2°N (almost half the peak upwelling velocity at 50 m on the equator due to wind) compensated by weaker downwelling at about 2°S and 5°N. This eddy-driven meridional circulation largely explains the meridional asymmetry in climatological mean equatorial Pacific upwelling.

SIGNIFICANCE STATEMENT: Global coupled atmosphere-ocean models have difficulty forecasting subseasonal to seasonal weather, in part due to difficulties simulating and observing upwelling in the equatorial Pacific ocean. High resolution regional ocean models and observations reveal a previously unknown meridional asymmetry in the upwelling in the Pacific as well as its physics. This discovery has the potential to guide future observations and model development that could improve subseasonal to seasonal predictions of the ocean and the weather.

1. Introduction

Upwelling along the equator in the central and east equatorial Pacific maintains and modulates the relatively cold sea surface temperatures, high nutrients and high partial pressure of carbon dioxide (Cromwell 1953; Bjerknes 1966; Wyrtki 1981). Hence, the associated vertical velocity and its detailed spatiotemporal structure are exceptionally important for global weather, climate and Earth system dynamics (McPhaden et al. 2006).

Although the detailed spatial structure of the climatological upwelling is not well constrained by observations, upwelling is usually understood to be centered on the equator and roughly symmetric meridionally across the equator. This circulation can be separated into three parts (e.g. Wyrtki 1981). The divergent poleward Ekman transport (1) north and south of the equator owing to the easterly winds is largely compensated by an equatorward geostrophic convergence (2) that extends deeper (to ∼ 200 m) than the Ekman layer (∼ 50 m) resulting in a meridional overturning circulation. The geostrophic convergence is reflected in the downward slope in the dynamic height and corresponding upward slope of the thermocline from west to east that arises from easterly winds along the equator. The zonal winds and meridional Ekman divergence are strongest in the central Pacific (from 140°W-170°W), where upwelling is also presumably strongest. There is also convergence of the zonal currents (3) below the mixed layer and divergence above. But, the zonal component of the divergence/convergence is smaller than the meridional component and contributes less than a quarter of the maximum mean upwelling.

This qualitative description as well as quantitative estimates of the large scale upwelling by Wyrtki (1981) are to first approximation confirmed by subsequent studies that used tracer budgets (Quay et al. 1983), arrays of moored current profiles (Halpern and Freitag 1987; Halpern et al. 1989; Weisberg and Qiao 2000), surface drifters (Poulain 1993; Karnauskas 2025), or syntheses of observations from various sources (Bryden and Brady 1985; Meinen et al. 2001) including multiple sections of direct velocity measurements collected by ship (Johnson et al. 2001). But, these observational studies do not quantify all the detailed spatial structure of the upwelling, and none of these studies suggest the upwelling is meridionally asymmetric.

Yet, it is well known that cold tongue sea-surface temperatures are meridionally asymmetric and cooler south of the equator in the east. Prior studies suggest that this southward shift of the cool sea-surface temperatures in the east is partly due to an inferred southward shift in peak upwelling, both of which are driven by the fairly strong southerly component of the wind in the east (Philander and Pacanowski 1981; Mitchell and Wallace 1992; McPhaden et al. 2008). However, the spatial relationship between sea-surface temperature (SST) and upwelling is not necessarily one-to-one. Other processes, such as poorly constrained mesoscale and submesoscale ocean eddy transports and turbulent vertical mixing (e.g., Moum et al. 2013; Wang et al. 2022; Liu et al. 2025) and atmospheric processes (e.g. cloud physics, see Cronin et al. 2006), are likely important. A perplexing example of the spatial mismatch between mean SST and upwelling is shown in an eddy resolving ocean model that simulates peak upwelling at 50 m depth off the equator at 1°N in the central Pacific, where the cold tongue SST is fairly symmetric about the equator and the winds do not readily explain a northward shift in upwelling (Fig. 2d of Deppenmeier et al. 2021). In this paper, we investigate the spatiotemporal structure and dynamics of the upwelling in the Pacific cold tongue in a high-resolution three-dimensional regional ocean circulation model. Motivated by the meridional asymmetry in eddy activity, which is also considerably stronger in the north (e.g., Chelton et al. 2000), we consider the hypothesis that this northward-shifted upwelling is due to eddy activity.

In the equatorial Pacific, tropical instability waves (TIWs) are the dominant eddies, and they are also a source of fluxes of momentum and buoyancy with a significant rectifying effect on the mean state (e.g., Hansen and Paul 1984). Bryden and Brady (1989) attempted to quantify the net upwelling on the equator owing to TIWs and found it to be an order of magnitude smaller than the observed mean upwelling, but their observations and analysis did not extend off the equator. McWilliams and Danabasoglu (2002) used the Gent and Mcwilliams (1990) parameterization to show that eddy driven upwelling is a significant but not dominant part of the equatorial meridional overturning cells. However, the Gent and Mcwilliams (1990) scheme was designed to mimic the impacts of midlatitude eddies, but tropical instability waves are different from midlatitude mesoscale eddies in their energetics and dynamics (Yu et al. 1995; Proehl 1998; Qiao and Weisberg 1998; Holmes et al. 2014). Using eddy-permitting models (at 0.25°-0.5° resolution), Hazeleger et al. (2001) and Richards et al. (2009) compared depth and isopycnal vertical coordinate averaging to show that eddy-driven mass transport opposes and compensates a narrow and shallow mean equatorial meridional overturning cell within about 5° of the equator (note these equatorial Hazeleger et al. (2001) cells are much narrower meridionally than the subtropical cells). Perez et al. (2010) compared averaging in a frontal and geographic meridional coordinate in a model and observations to show that tropical instability waves have a considerable rectified effect on the mean upwelling and meridional circulation. Maillard et al. (2022) used a creative online filtering approach to generate a counterfactual simulation without TIWs and thereby quantify the rectified effect of tropical instability waves on the mean state in an eddy-resolving (1/12°) regional simulation. They found that tropical instability waves strengthen the poleward meridional velocity in the upper 50 m between 1-6°N and 1-5°S thus increasing the mean equatorial divergence, consistent with Hazeleger et al. (2001) and Richards et al. (2009). Hence, there is evidence from observations and simulations that the eddies significantly alter the mean meridional circulation in the equatorial Pacific cold tongue.

Here, a linear diagnostic Eliassen (1951) model for the zonal-mean meridional circulation is used to isolate the eddy-driven part of the upwelling from the dominant wind driven part in the simulation. Eliassen (1951) originally developed the model of a slow frictionally or diabatically driven axisymmetric meridional circulation in a balanced vortex to theoretically investigate the potential mechanisms and structure of the meridional circulation in the midlatitude atmosphere. Shapiro and Willoughby (1982) and others have used the Eliassen models to understand the axisymmetric secondary circulation and evolution of balanced hurricane-like vortices in response to sources of azimuthal momentum and heat. In the ocean, Niiler (1969), Garrett and Loder (1981), Flierl and Mied (1985), Thompson (2000), Whitt et al. (2017), Crowe and Taylor (2018) and others have used similar models to understand vertical circulations at midlatitude ocean fronts and mesoscale eddies driven by air-sea fluxes and turbulent mixing. The Eliassen model can also be viewed as a reduction of the "generalized omega equation" (Thomas et al. 2010; Giordani et al. 2006), which yields the secondary circulation in response to both quasi-geostrophic frontogenesis (or frontolysis) (Hoskins 1982; McWilliams 2021) and sources and sinks of momentum and buoyancy. Almost all of the prior applications use the Eliassen model in the midlatitudes and most focus on frontogenesis rather than mixing and surface sources and sinks of momentum and buoyancy (such as the wind forcing). The lack of prior applications to equatorial upwelling is presumably a reflection of the low Coriolis frequency and reduced prominence of geostrophic balance as well as the lack of information about the eddy-driven sources and sinks of zonal momentum and buoyancy.

The outline of the paper is as follows. The description and evaluation of the upwelling in the numerical ocean simulation is in section 2 and the Appendix, the theory behind the decomposition of upwelling by process (the Eliassen model) is presented in section 3, and the results of that decomposition are in section 4. Throughout the paper, the term "Eliassen model" or "model" refers to the linear two-dimensional Eliassen model described in section 3, and the terms "general circulation model" (gcm) and "simulation" refer to the three-dimensional regional ocean gcm and its output, which are described in section 2.

2. Description of the upwelling in a numerical simulation

a. Simulation setup and gcm description

A submesoscale permitting numerical simulation of the region from 12°S-12°N and from 95°W-170°W over the period from 1999-2018 (previously published in Whitt et al. 2022) is used to study the meridional circulation and upwelling in the equatorial Pacific. The longitude range was chosen to approximately span the cold tongue west of the Galapagos Islands; it is the same range used in the observational analysis of the cold tongue upwelling by Johnson et al. (2001). The temporal range includes the major 2015-2016 El Niño event (Niño 3.4 Index>1) as well as more modest events in 2009-2010, 2006-2007, and 2002-2003 (Niño 3.4 Index>1). It includes the tail end of the 1998-1999 La Niña as well as the 2007-2008 event and double dip 2010-2012 and 2016-2018 events. The mean Niño 3.4 Index during the simulated period (1999-2018) is -0.13 based on the ERSSTv5 dataset (Huang et al. 2017).

The simulation is performed using the Massachusetts Institute of Technology general circulation model (MITgcm), which numerically solves the hydrostatic primitive equations (Marshall et al. 1997; Adcroft et al. 2004). The simulation is executed on a 1/20°-resolution grid with 100 evenly spaced layers in the top 250 m (at 2.5 m resolution) and 85 more layers telescoping from 2.5 m thick at 250 m depth to 100 m thick at 5750 m depth. The ocean lateral boundary conditions from the daily outputs of the Copernicus global 1/12°-resolution ocean reanalysis (GLORYS12) (Lellouche et al. 2021), which resolve the equatorial zonal jets and tropical instability waves, are imposed by relaxing to boundary values in a sponge layer with timescales ranging from 4 hours at the boundary to 10 days 1.5° from the boundary. The outgoing radiative heat fluxes as well as the turbulent air-sea fluxes of heat and momentum as well as evaporation of freshwater are calculated online using bulk formulas from near-surface atmospheric fields from the 3-hourly 0.5°-resolution bias-corrected Japanese Reanalysis ocean forcing dataset (JRA55-do) (Tsujino et al. 2018) and simulated SST. JRA55-do also specifies downwelling longwave radiation, downwelling shortwave radiation that penetrates and warms the interior ocean, as well as a surface precipitation flux. The K-profile parameterization is used to represent turbulent vertical mixing (Large et al. 1994).

Daily averages of temperature, salinity, sea surface height and all three components of velocity were saved. Some surface fluxes, e.g. of heat and momentum, along with the three-dimensional budget diagnostics for both components of horizontal velocity and temperature were saved as well. A 2° wide buffer on all sides of the model domain is excluded from the analysis to avoid the sponge region.

The simulated hydrography (Figs. A1-A2) and horizontal velocity (Figs. A3-A7) are shown to be broadly realistic in a comparison to observational products in the Appendix. A notable discrepancy is a weaker mean poleward surface flow off the equator; between 2°S and 4°S the simulated velocities are about 30% weaker than observational estimates (Fig. A5). The simulated variances of the sea-surface height (Fig. A8) and horizontal velocities (Fig. A9) are also qualitatively realistic but weaker than observed. In addition, the mixed layer depth, surface heat flux, and subsurface turbulent heat fluxes near the mixed layer depth are discussed in Whitt et al. (2022). Mixed layer depths and surface heat fluxes are fairly realistic, and simulated turbulent heat fluxes near the mixed layer base at 0,140°W are stronger than observed by a factor of 2-3 on average but have a realistic seasonal cycle. Thus, these simulations provide a reasonably realistic estimate of the climatological equatorial Pacific circulation with dynamically consistent and qualitatively realistic fine-scale structure down to horizontal scales of order 10 km and timescales of a few days.

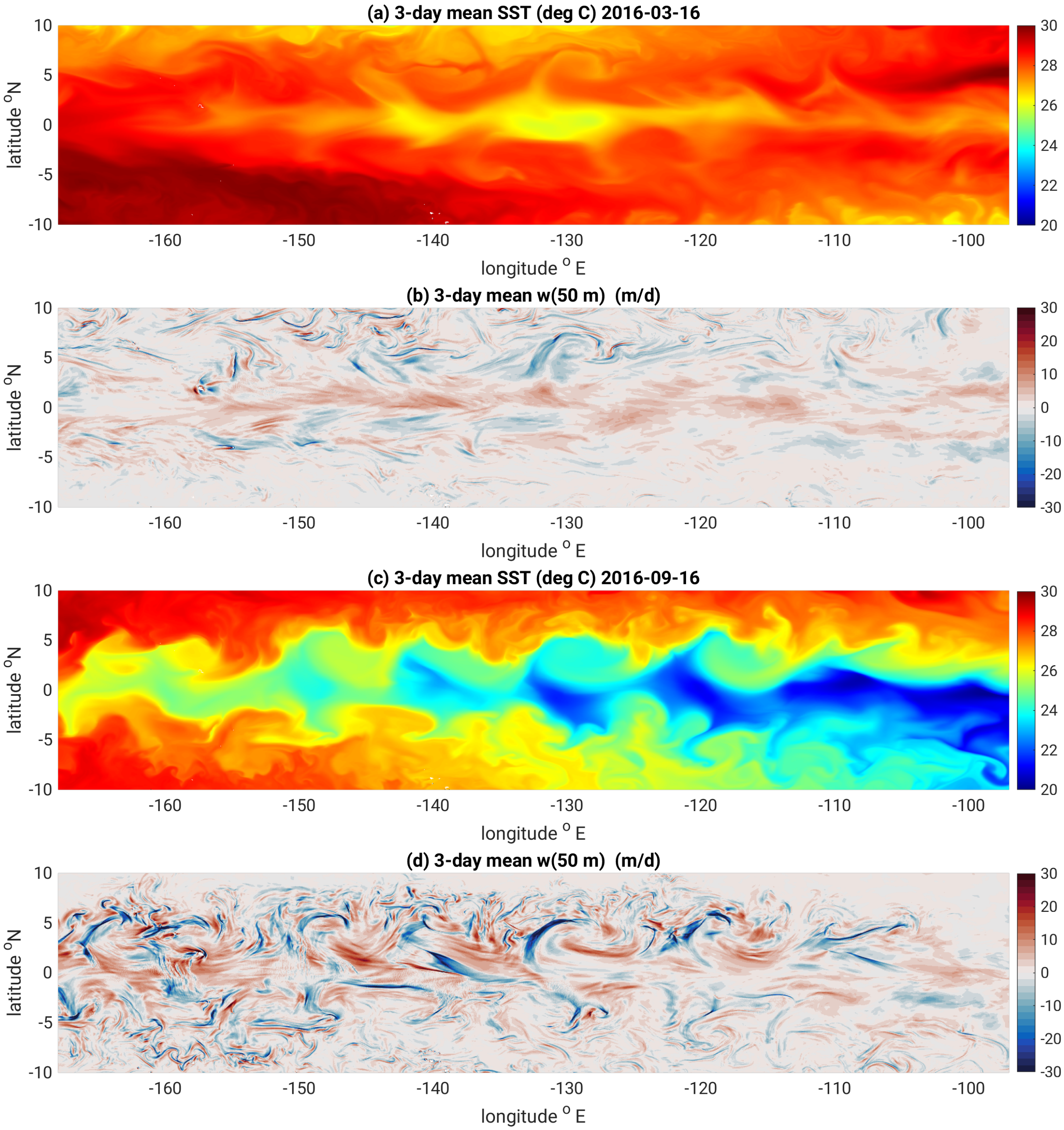

Fig. 1. Representative maps of the simulated SST and vertical velocity at 50 m depth averaged over three days in March and September 2016 during the transition from a strong El Niño to a weak La Niña. Eddy activity is relatively weak in (a)-(b) and relatively strong in (c)-(d), highlighting the impact of the seasonal cycle.

b. Transient modulation of upwelling by tropical instability waves and submesoscale fronts

The vertical velocity at 50 m is highly variable in space and time (Figs. 1b,d) and modulated seasonally, interannually, and—perhaps most dramatically—by tropical instability waves at intraseasonal timescales (TIW; Fig. 1c-d; compare to e.g. Chelton et al. (2000)). Averaged over three days, the vertical velocity at 50 m has characteristic magnitudes of 10-20 m/d, much larger than typical estimates of the peak in time-mean upwelling of 1-3 m/d (Bryden and Brady 1985; Halpern and Freitag 1987; Meinen et al. 2001; Johnson et al. 2001). The vertical velocity is far more variable in boreal fall and especially during La Niña when TIWs are strong compared to boreal spring and El Niño when TIWs are weak. During boreal fall, strong downwelling tends to be associated with fronts on the northwestern edges of TIWs, while upwelling tends to be strongest in TIW troughs. In addition, strong submesoscale upwelling and downwelling is often associated with fronts on both the northern and southern flanks of the cold tongue. The magnitude of the transient vertical velocities during boreal fall (Fig. 1d) are qualitatively consistent with observational estimates of about 10 m/d from an array of mooring observations spanning 4° zonally and 2° meridionally near 140°W on the equator in fall of 1990 (Weisberg and Qiao 2000).

During boreal spring, in contrast, the simulated transient vertical velocities are weaker, ranging from $1-10$ m/d, and more similar in magnitude and spatial structure to estimates of the climatological mean upwelling (Fig. 1b). For example, the upwelling is enhanced in a patchy but zonally-coherent band about 5° wide along the equator in the central Pacific (Figs. 1a-b). Similarly, there is no evidence of the oscillatory strong vertical velocities attributed to tropical instability waves outside of the Boreal fall in the observations of Weisberg and Qiao (2000).

c. Regionally-integrated upwelling

Climatological upwelling integrated over a large region encompassing the cold tongue can be quantified by combining wind stress (Ekman transport) along with hydrography (geostrophic transport) to build an indirect mass balance following Wyrtki (1981). Observation-based and simulation-based estimates are compared in a Wyrtki diagram focusing on upwelling at 50 m in Fig. 2. The upwelling is calculated in a box spanning 97°W to 168°W and 5°S to 5°N.

In the Wyrtki diagram (Fig. 2), the observed meridional geostrophic transports at 5°N and 5°S are derived by vertically integrating the zonal dynamic height differences in Fig. A2,

$$M_g^y = -\frac{g}{f}\int D_{168W} - D_{97W}\, dz. \tag{1}$$

The dynamic height D is calculated from the 1/6°-resolution Argo climatology (2004-2018) of Roemmich and Gilson (2009) and referenced to 500 m depth. The observed meridional Ekman transports at 5°N and 5°S are given by

$$M^y_{Ek} = -\int_L \frac{\tau_x}{\rho_0 f} dx, \tag{2}$$

where the zonal stress τ_x is from the 1/4°-resolution QuickSCAT scatterometer climatology of the surface wind stress by Risien and Chelton (2008). In these calculations, $g = 9.81$ m/s^2 is a constant acceleration due to gravity, $\rho_0 = 1025$ kg/m^3 is a constant reference potential density, L is the zonal extent of the domain at ±5°N, and $f = 14.6 \times 10^{-5} \sin(\pm 5°)$ is the Coriolis frequency at ±5°N. The Ekman transport is assumed to occur entirely in the top 50 m. The observational estimates of the zonal divergence are obtained by volume integrating $\partial_x u$, which is estimated at each depth and latitude from the slopes of linear fits to the mean zonal velocity u in the box. These observational estimates of $\partial_x u$ are from two independent sources: first, the TAO moored ADCP observations on the equator at 110°, 140°, and 170°W (McPhaden et al. 2010) merged with geostrophic velocities (Roemmich and Gilson 2009) off the equator (Argo+MADCP) and, second, the repeat shipboard ADCP observational (SADCP) climatologies of zonal velocity in 6 sections spanning our box (Johnson et al. 2002). All of these observations are visualized and described in more detail in the Appendix. The upwelling across 50 m is then estimated by summing the meridional Ekman divergence (positive), the meridional geostrophic convergence over the top 50 m (negative), and the zonal divergence over the top 50 m (positive) to obtain the upwelling across 50 m required for mass balance. Subsequently, the meridional geostrophic convergence between 50 and 200 m and the zonal convergence between 50 and 200 m are subtracted from the upwelling across 50 m to obtain an estimate of the upwelling at 200 m required for mass balance. The upwellings across 50 m and 200 m are similarly calculated in the gcm from the surface stress, hydrography, and zonal velocity using mass balance. All the simulated meridional and vertical transports are also calculated *directly* by integrating the velocity on the box edges to evaluate the errors in the indirect estimates based on wind stress, hydrography and mass balance. Finally, we compare our new observational and simulation based transports to the transports in Wyrtki (1981). The box used here is slightly smaller than Wyrtki's, which spanned 100°W to 170°E, so we multiply his

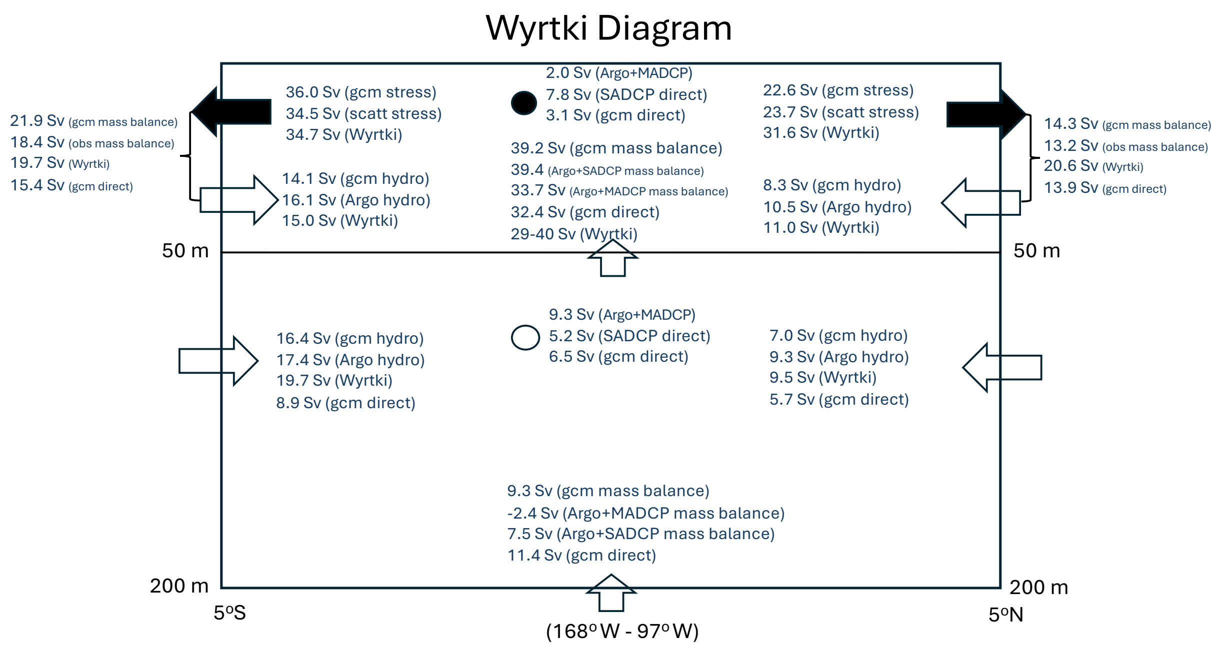

FIG. 2. The Wyrtki diagram (as in Wyrtki 1981) quantifies the bulk volume budget in a box between 97°W and 168°W and from 5°S to 5°N. The solid and open circles indicate zonal divergence (net outflow) above 50 m and convergence (net inflow) from 50-200 m, respectively. The label "mass balance" refers to the transports calculated by indirect mass balance based on hydrography and wind stress as described in the text. The label "Wyrtki" indicates the rescaled mass balance estimates from Wyrtki's (1981) paper (his Fig. 5); the meridional transports are from his Figs. 5b-c. The label "hydro" indicates that the transports are geostrophic (hydrography). The label "direct" indicates the transports are from velocities. The label "scatt" is short for scatterometer.

results (in his Fig. 5b-c) by the ratio of box lengths (71°/90°) for comparison with the simulation used here (Fig. 2).

The Wyrtki diagram quantifies the similarities and differences between the simulation and the observational products at the regional scale of the box (Fig. 2). The mass balance estimates of upwelling at 50 m range from 34 to 39 Sverdrups (1 Sv = 10^6 m^3/s). These estimates are within the range of estimates given by Wyrtki (1981) (29-40 Sv, in his Figs. 5a-c). The simulated meridional Ekman transports are very similar to observations (Risien and Chelton 2008; Tsujino et al. 2018). The simulated equatorward geostrophic transports are consistent with the Argo observations to within 10-30%, but systematically weaker. This weakness reflects the weaker zonal dynamic height gradient in the gcm compared to Argo (Fig. A2). Despite considerably less data, Wyrtki (1981) generally found similar meridional transports. However, Wyrtki found that the Ekman transport at 5°N was about 40% stronger than in the climatology of Risien and Chelton (2008). Yet, Wyrtki (1981) provided a wider range of upwelling estimates (29-40 Sv), mainly due to uncertainty about the vertical structure of zonal divergence/convergence.

The zonal divergence $\partial_x u$ remains an important uncertainty in the regionally integrated volume budget because $\partial_x u$ must be integrated across the equator where geostrophic and Ekman transports cannot be used. In Fig. 2, this uncertainty is reflected in the considerable difference between the observational estimates of zonal divergence (outflow) above 50 m (see also the Appendix and Figs. A3 and A4). The zonal convergence (inflow) from 50-200 m is somewhat more robust, perhaps because both the moored and shipboard ADCP observations are available below 30 m but not above. Nevertheless, uncertainty in zonal divergence above 50 m amounts to only 10-20% (roughly 5 Sv), because upwelling at 50 m is dominated by meridional divergence.

We further quantify the uncertainties in the meridional and vertical transports by evaluating the accuracy of the mass balance method in the simulation (Fig. 2). The upwelling at 50 m calculated directly by integrating w is 32 Sv versus 39 Sv by mass balance, suggesting the mass balance upwelling is quantitatively accurate to 20%. In the gcm, the stronger mass balance upwelling at 50 m is linked to stronger southward transport above 50 m depth at 5°S from the sum of the Ekman and geostrophic parts, which are together 6.5 Sv (40%) larger than the actual southward transport of 15.4 Sv. This difference is largely compensated in the transports from 50 m to 200 m depth at 5°S, where the geostrophic northward transport is 7.5 Sv (~80%) larger than the true northward transport of 8.9 Sv. These vertically compensating transport discrepancies are also found at 5°N but are much smaller there. A possible explanation is that the Ekman layer extends below 50 m, especially in the southern hemisphere where mixed layers are somewhat deeper (MLD is shown in Fig. 5e of Whitt et al. 2022).

At 200 m depth, the simulated upwelling is 11.4 Sv by direct integration of w and 9.3 Sv by indirect mass balance. The observational mass balance estimates are somewhat lower but range more widely from -2.4 Sv (downwelling) to +7.5 Sv (upwelling). Other observational estimates over narrower latitude ranges also suggest downwelling below the Equatorial Undercurrent (EUC) core, so the estimated downwelling of 2.4 Sv using the Argo+MADCP zonal divergences cannot be dismissed (Bryden and Brady 1985; Halpern and Freitag 1987; Weisberg and Qiao 2000; Meinen et al. 2001). The meridional geostrophic and zonal convergences between 50 and 200 m exhibit only modest differences between the simulation and observations (~ 1 to 3 Sv). But these modest differences in the convergences from 50 to 200 m combined with differences in upwelling at 50 m of about 5 Sv yield the fairly wide range of estimates in upwelling at 200 m. While the simulated upwelling at 200 m at 11 Sv is higher than all of the observational estimates, we cannot confidently say the simulated upwelling at 200 m is unrealistic due to large observational and methodological uncertainties.

d. Spatial structure of the mean upwelling

The simulated time mean upwelling is to first order zonally uniform (Fig. 3c-d), about 4° wide and centered on the equator with peak upwelling of 1-2 m/d just above 100 m depth (Fig. 3a), roughly consistent with observations and established understanding (Bryden and Brady 1985; Poulain 1993; Halpern and Freitag 1987; Halpern et al. 1989; Weisberg and Qiao 2000; Meinen et al. 2001; Johnson et al. 2001). Averaged from 2°S to 2°N at 50 m, the upwelling peaks in the central Pacific at about 1 m/d near 145°W and decays to about 0.5 m/d by 97° W and 168° W (Fig. 3c-d), qualitatively consistent with the zonal variation of the zonal wind stress.

The simulated vertical velocity at 50 m (w_{50}) is meridionally asymmetric (Fig. 3a-c). The asymmetry is calculated as the cross-equatorial difference in w_{50} at each latitude (northern hemisphere minus southern hemisphere; see Fig. 3b). We plot the latitude of maximum asymmetry in both hemispheres on maps (e.g., the magenta dots in Fig. 3c) to highlight the fact that the asymmetry is defined as a difference between hemispheres. The latitude of maximum asymmetry in w_{50} occurs about 2° from the equator (Fig. 3b) across longitudes but occurs slightly (~50 km) nearer to the equator west of 130°W (as shown in Fig. 3c). Hence, w_{50} is greater at 2°N than 2°S at essentially all longitudes, although the magnitude of this asymmetry in w_{50} decreases zonally towards the east

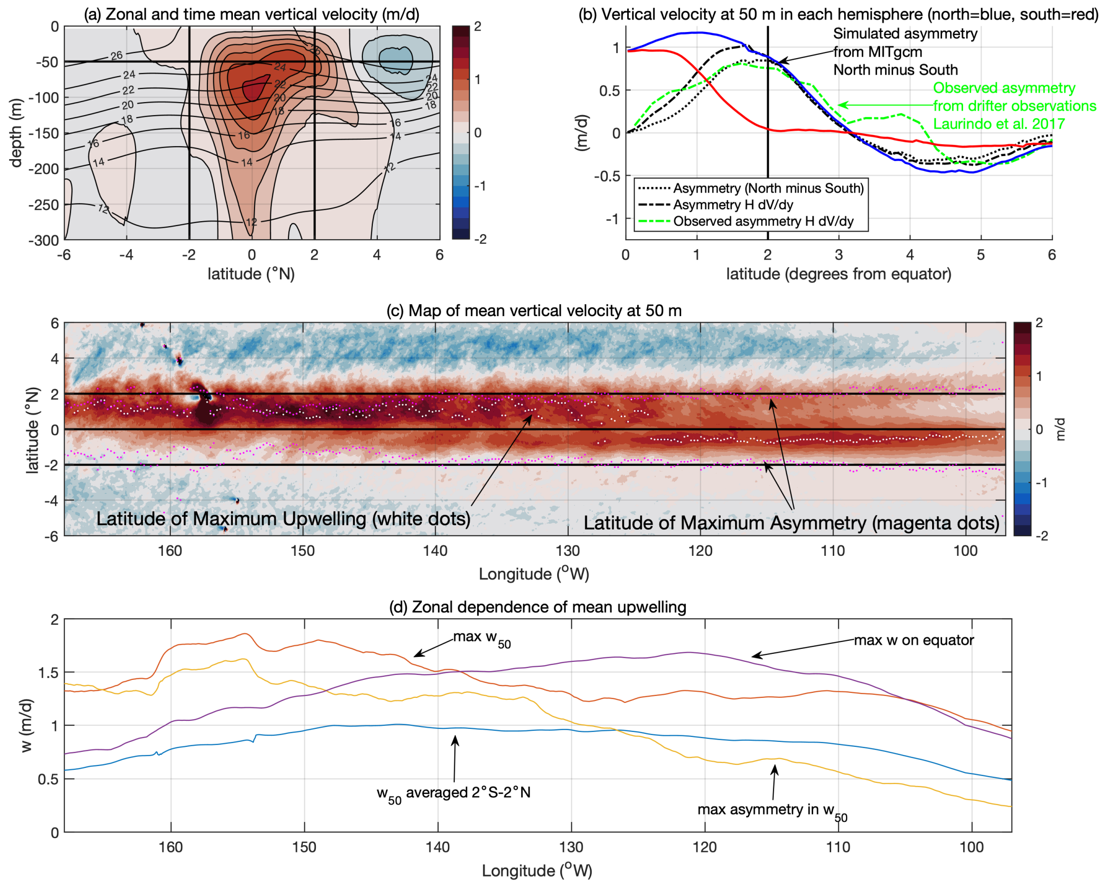

FIG. 3. Simulated time mean vertical velocity w in meters per day (m/d) in the MITgcm, including a zonal mean section averaged from 97-168°W in (a) and a map at 50 m depth w_{50} in (c). (b) shows the meridional asymmetry in w_{50} that is the difference between hemispheres by latitude (north minus south). The black and green dash-dotted lines in (b) are derived from the meridional divergence $\partial_y v$ at 15 m scaled to a vertical velocity estimate at 50 m by multiplying by $H = 35$ m (black from the gcm, green from the gridded drifter observations of Laurindo et al. (2017)). The white dots in (c) denote the latitude of maximum w_{50} while the magenta dots denote the latitude of maximum asymmetry in w_{50} (i.e., of maximum difference between hemispheres). The thick straight black lines in all plots are just for reference: at 2°, the equator, and 50 m depth. In (d), the three-dimensional w is smoothed with a 7° zonal moving average and various measures of the zonal variation of upwelling are calculated ("on the equator" is an average from 0.05°S to 0.05°N).

from about 1.5 m/d near 160°W to 0.25 m/d near 100°W (yellow line in Fig. 3d). The zonal mean upwelling at 50 m also reaches a maximum north of the equator (Fig. 3a-b), in contrast to the typical assumption that upwelling peaks on the equator and especially the inferences from drifter observations (Poulain 1993; Karnauskas 2025) (see also the Appendix and Fig. A5b). However, the latitude where w_{50} reaches a maximum (white dots in Fig. 3c), which is not necessarily co-located with a latitude of maximum asymmetry in w_{50}, shifts from about 1°N west of 130°W to 0.5°S east of 130° W. The magnitudes of these maxima in mean w_{50} decay from about 1.75 m/d near 150-160°W in the central Pacific to 1 m/d at 100°W in the east Pacific (red line in Fig. 3d).

The shift of the maximum in w_{50} to 0.5°S in the east may partially reflect the stronger southerly winds there (Mitchell and Wallace 1992; Philander and Pacanowski 1981). But peak meridional asymmetry in w_{50} near 2° is stronger in the central Pacific than the east Pacific and is qualitatively similar in both the central and east Pacific, whereas the meridional wind is stronger in the east Pacific than in the central Pacific. Hence, the peak asymmetry in w_{50} and stronger upwelling in the northern hemisphere near 2° is likely unrelated to the meridional wind.

The meridional asymmetry in upwelling is missing in observational estimates that usually could not make fine latitude distinctions. However, the observations of the climatological meridional velocity at 15 m from the global drifter program (Laurindo et al. 2017) have fine enough meridional resolution and sufficient data to reveal very nearly the same off-equatorial meridional asymmetry in zonal mean meridional divergence $\partial_y v$ as in the simulation (Fig. 3b; c.f. green and black dash-dotted lines). See the Appendix and Figs. A5-A6 for further discussion and plots of the meridional divergence. The simulated $\partial_y v$ in turn has a very similar meridional asymmetry as w_{50} (Fig. 3b; c.f. the black dash-dotted and dotted lines). The pattern correlation between mean $\partial_y v$ at 15 m and w_{50} is $r^2 = 0.98$ and the slope = 36 m for a regression spanning 4°S - 6°N. The slope of the regression of w_{50} on $\partial_y v$ represents a vertical depth scale in meters, which is roughly the thickness of the Ekman layer. In addition, Fig. 7d of Karnauskas (2025) and Fig. 2d of Deppenmeier et al. (2021) show a qualitatively similar meridional asymmetry in mean w_{50} near 2° in two different high resolution global ocean simulations, including the 1/12° GLORYS reanalysis and a 1/10° Parallel Ocean Program hindcast. These results suggest that the simulated meridional asymmetry in off-equatorial upwelling is a feature of the real ocean (Fig. 3b).

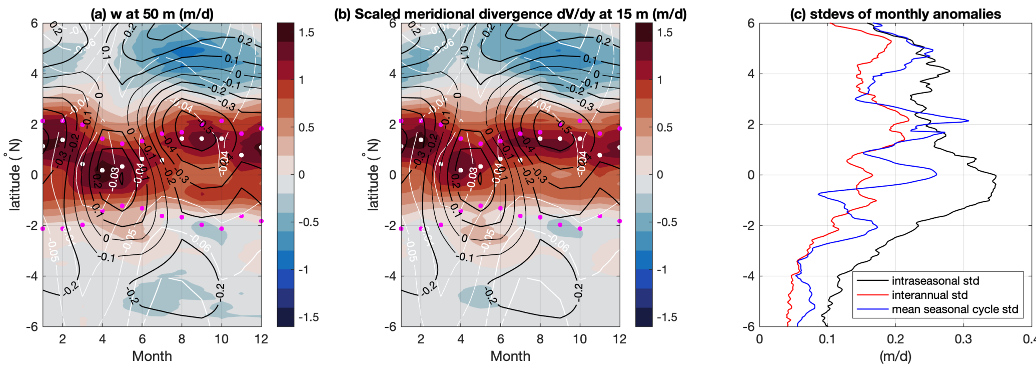

FIG. 4. Simulated seasonal cycle of the zonal mean vertical velocity at 50 m w_{50} in the MITgcm (a), the zonal mean meridional divergence $\partial_y v$ at 15 m multiplied by $H = 35$ m (b), and (c) a comparison between standard deviations in w_{50} associated with the mean seasonal cycle (blue) and intraseasonal (black) and interannual (red) monthly anomalies from the mean seasonal cycle. The interannual is separated from the intraseasonal using a 9-month running mean. In (a) and (b), the white dots are the latitudes where w_{50} is maximum, the magenta dots are where meridional asymmetry in w_{50} is maximum, the white contours are of zonal wind stress (every 0.01 N/m^2), and the black contours are of zonal velocity at 15 m (every 0.1 m/s).

e. Seasonal cycle of upwelling

To first order, the simulated upwelling has roughly the same maximum zonal mean w of about 1-2 m/d, meridional width of about 4°, and location (within 2° of the equator and between 50-100 m depth) throughout the climatological year (Figs. 4-5). The seasonal variations in w are small. The standard deviations associated with the seasonal cycle of the zonal mean w_{50} (0.1-0.3 m/d) are considerably smaller than the annual mean w_{50} within 2° of the equator (1-1.5 m/d; Fig. 4c). The regionally integrated w_{50} within 2° of the equator varies seasonally by only about 25% from a minimum of 30 Sv in early boreal fall (August-October) to a maximum of 38 Sv in boreal winter (January-March). The seasonal cycle in upwelling is surprisingly small given that the zonal wind stress on the equator increases by almost a factor of two from 0.025 N/m^2 in Boreal spring to 0.045 N/m^2 in early autumn (white contours in Figs. 4a-b) when the sea-surface temperature on the equator declines by about 2°C (not shown). Integrating w_{50} between 5°S and 5°N results in a larger seasonal cycle that varies from 42 Sv to 22 Sv, mainly due to the seasonal cycle in downwelling between 2-5° from the equator in both hemispheres.

The meridional asymmetry in the zonal mean w_{50} also has a large seasonal cycle (Figs. 4-5). The maximum meridional asymmetry in w_{50}, which is otherwise about 1 m/d, weakens considerably in boreal spring to a minimum of about 0.3 m/d (Figs. 4-5), because the seasonal cycle in w_{50} is out of phase between the equator and 2°N. On the equator, zonal mean w_{50} achieves its annual maximum of about 1.5 m/d in boreal spring, and achieves its annual minimum of about 0.6 m/d in boreal autumn, approximately in phase with the regional integrals of w_{50}. In contrast, at 2°N, w_{50} achieves its annual maximum of 1.25 m/d in boreal winter, and achieves its annual minimum of 0.4 m/d in boreal spring.

As expected, the meridional divergence $\partial_y v$ above 50 m has a very similar seasonal cycle and meridional asymmetry as w_{50} (c.f., Figs. 4a-b). The pattern correlation between the zonal mean w_{50} and zonal mean $\partial_y v$ at 15 m is high, $r^2 = 0.68$ and the slope = 36 m for a regression spanning 4°S - 6°N after the annual means are removed from both variables. The simulated seasonal cycle in meridional velocity at 15 m between 2-8°N is similar to the drifter-based observational product (Fig. A7a-b). But the uncertainties are too large to evaluate the simulated seasonal cycle of v and $\partial_y v$ within 2° of the equator using the observational product of Laurindo et al. (2017) (Fig. A7c).

f. Modulation of upwelling by El Niño and other variability

The regionally integrated upwelling (from 5°S to 5°N) varies by about 20 Sv from its minimum in late 2015 (El Niño) to its maximum in late 2016 (La Niña) (Fig. 6a). The 2015-2016 ENSO event also significantly impacted the meridional asymmetry of upwelling (Fig. 7). Compared to the 2016 La Niña, the zonal and time mean upwelling at 50 m is reduced by 0.5 m/d near 2°N and the downwelling is reduced by about 0.5 m/d near 5°N during the 2015 El Niño. But, there was comparatively little difference in w_{50} in the Southern Hemisphere between El Niño and La Niña. Hence, the asymmetry is substantially reduced during the El Niño reaching a maximum of only about 0.5 m/d at about 1.5° from the equator, while the asymmetry is enhanced during the La Niña reaching a maximum of about 1.5 m/d about 2-3° from the equator. Consistent with the major 2015-2016 ENSO event, there is also reduced upwelling near 2-3°N and reduced meridional asymmetry in w_{50} during El Niño and vice versa during La Niña (Figs. 6b-c) in the 2006-2007 and 2009-2010 ENSO events.

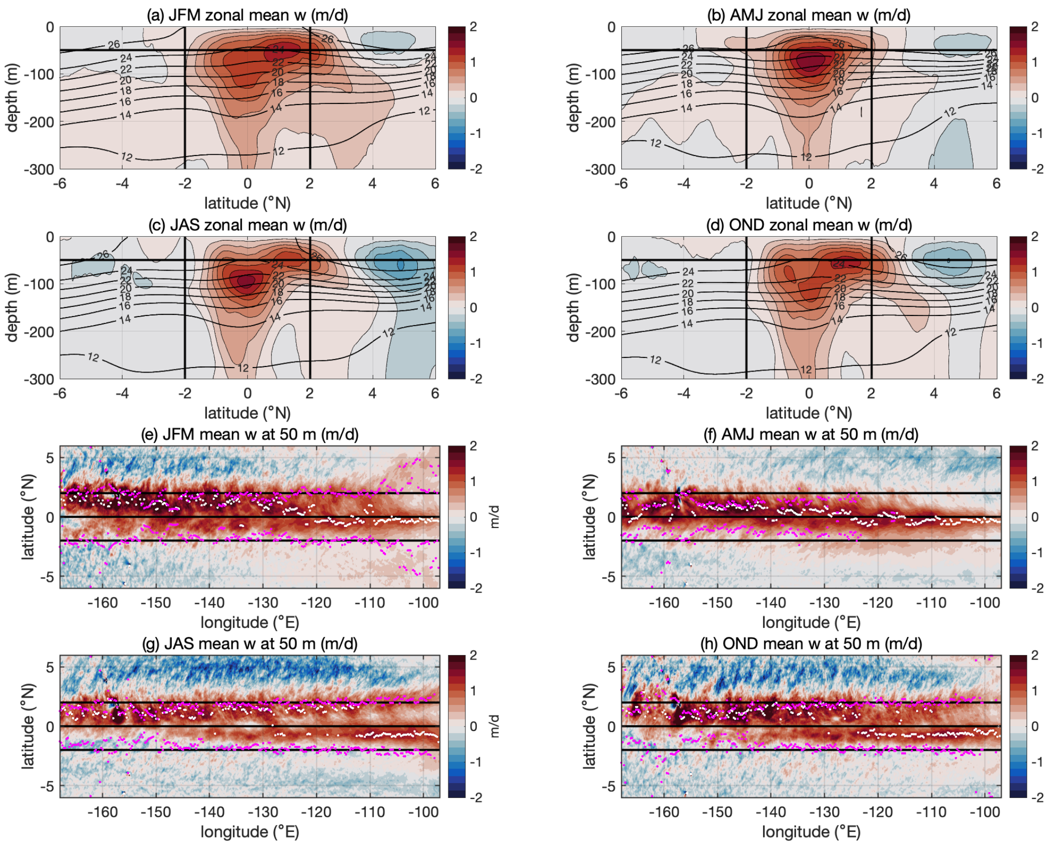

FIG. 5. Simulated climatological seasonal cycle of the vertical velocity in the MITgcm averaged zonally and seasonally: in (a) January, February, March (JFM); (b) April, May, June (AMJ), (c) July, August, September (JAS), and (d) October, November, December (OND). (e)-(h) show maps of climatological w at 50 m in each season. The plots in (a)-(d) are analogous to Fig. 3a and (e)-(h) are analogous to Fig. 3c, where further description can be found.

Despite the apparent impact of ENSO on the interannual variability of w_{50} (Figs. 6a and Fig. 7), interannual anomalies are qualitatively and quantitatively modest in several ways. First, the standard deviation of interannual anomalies is comparable in magnitude to the standard deviation of the seasonal cycle and is significantly smaller than the standard deviation of intraseasonal variability (Fig. 4c). And all three of these standard deviations (interannual, seasonal, and intraseasonal) are considerably smaller than the mean upwelling of about 1 m/d within 2° of the equator. Excluding strong ENSO events, regionally integrated upwelling varies by only a few Sverdrups interannually

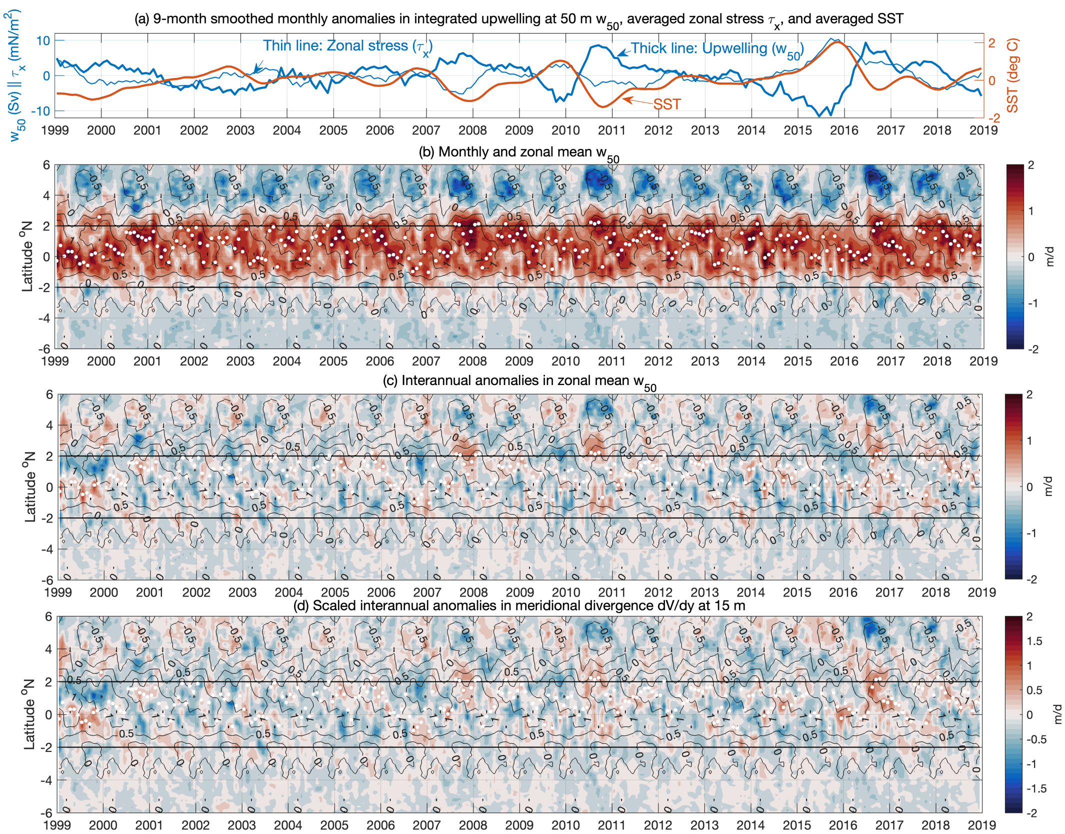

Fig. 6. (a) Time series of regionally averaged SST anomalies, regionally averaged zonal wind stress anomalies, and regionally integrated upwelling anomalies at 50 m in the MITgcm (as in Section 2c and Fig. 2), all of which are monthly deviations from the climatological seasonal cycle smoothed with a 9-month moving average. (b) is a Hovmoller diagram of the monthly and zonal mean w_{50}, (c) is a Hovmoller diagram of the corresponding monthly anomalies in w_{50} from the climatological seasonal cycle, and (d) is a Hovmoller diagram of the corresponding monthly anomalies in meridional divergence $\partial_y v$ at 15 m scaled by a constant $H = 35$ m to convert to a vertical velocity scale as in Fig. 4b. The monthly climatology of w_{50} is overlaid using black contours every 0.5 m/d for reference in (b)-(d). The white dots mark the latitudes of maximum zonal mean w_{50} in (b)-(d). The horizontal black lines 2° from the equator are just for reference.

(Fig. 6a). The interannual anomalies in upwelling evolve oppositely to the SST anomalies, similar to what occurs during ENSO events (Fig. 6a). The climatology is prominent in the Hovmoller

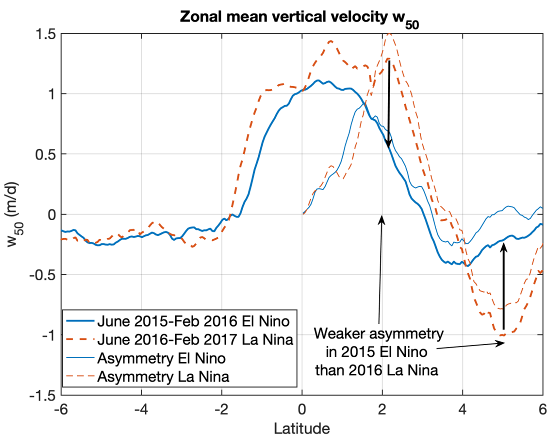

FIG. 7. Meridional profiles of the time and zonal mean vertical velocity at 50 m w_{50} in the gcm during the 2015-2016 El Niño (thick red dashed line) and the 2016-2017 La Niña (thick blue line). The corresponding asymmetries (northern hemisphere minus southern hemisphere) are plotted as thin lines of the same color and style in the northern hemisphere.

diagram of zonal mean monthly w_{50} (Fig. 6b), with climatological meridional asymmetry seen in most years.

Historical observations are inadequate to constrain the meridional structure of zonal mean w_{50} and the zonal mean near-surface meridional velocity during ENSO events. Nevertheless, it is valuable from the point of view of planning future observing efforts to note that the monthly anomalies in zonal mean w_{50} (Fig. 6c) vary coherently with the monthly anomalies in zonal mean $\partial_y v$ near the surface (Fig. 6d). The pattern correlation is $r^2 = 0.77$ and the slope = 33 m in a regression spanning 4°S - 6°N after the climatological seasonal cycles are removed, and $r^2 = 0.68$ for $\partial_y v$ at 1.25 m instead of 15 m. In addition, the impact of the 2015-2016 ENSO event on the meridional structure of near-surface meridional divergence is qualitatively the same as the impact on w_{50} in Fig. 7 (c.f. Figs. 6c-d). Thus, persistent and widespread observations of the horizontal velocity near the surface combined with a more limited array of observations of horizontal velocity profiles below the surface could potentially be used to test the hypothesis that ENSO modulates the meridional asymmetry of meridional divergence and/or upwelling as suggested by the gcm (Figs. 6-7).

3. Eliassen model of the time and zonal mean ageostrophic meridional circulation

In this section, we derive the Eliassen model that decomposes the process drivers of the time and zonal mean upwelling and meridional overturning circulation from the MITgcm output.

a. Motivation

The Eliassen model has primarily been applied to midlatitude atmosphere and ocean dynamics, where the secondary circulation and vertical motion are diagnosed as a restorative response to tendencies (in the horizontal vorticity) that disrupt a dominant flow in thermal wind balance (Eliassen 1951; Giordani et al. 2006; Thomas et al. 2010; Giordani and Caniaux 2011). However, equatorial currents are not necessarily in thermal wind balance owing to the rapid adjustment by equatorial trapped waves. Instead, we focus on the climatological time (1999-2018) and zonal (95°W-170°W) mean dynamics (denoted by an overbar). Then, the zonal velocity $\overline{u}$ is in thermal wind balance with the buoyancy $\overline{b} = -g\overline{\rho}/\rho_0$ (Fig. 8) as given by

$$f\partial_z\overline{u} \approx -\partial_y\overline{b}, \tag{3}$$

where ρ is the potential density (Fig. 8). We expect thermal wind balance to be dominant on timescales of months to decades. Hence, the methodology developed here can likely be applied to study seasonal and interannual variability as well as the 20-year time mean dynamics, but we leave an investigation of this variability to future work.

The Eliassen equation for the zonally averaged meridional circulation is derived from the governing equation for the zonal thermal wind *imbalance*, which is defined by

$$\phi \equiv f\partial_z u + \partial_y b. \tag{4}$$

The definition (4) also gives the sum of the two dominant terms in the budget for the time and zonal mean zonal vorticity $\overline{\omega_x}$ (Fig. 8). The budget equation for ω_x is obtained by applying $-\partial_z$ to the meridional momentum equation of the incompressible hydrostatic primitive equations and

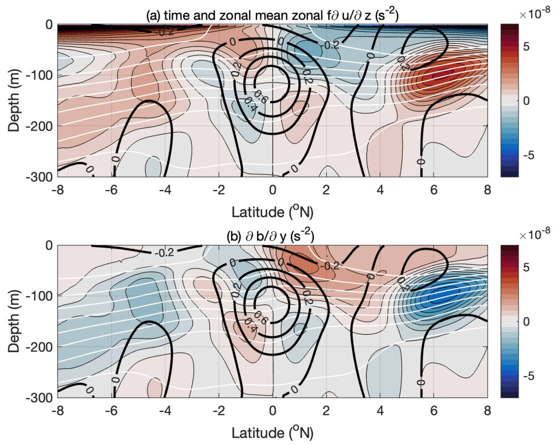

FIG. 8. The dominant terms in the time and zonal mean zonal vorticity dynamics in the MITgcm simulation: (a) tilting of planetary vorticity by the vertical shear of the zonal velocity $f\partial_z u$ and (b) the baroclinic torque $\partial_y b$. Below the top 25 m, they are very nearly equal and opposite, that is the mean zonal vorticity dynamics is dominated by thermal wind balance as given in equation (3). Black contours of zonal velocity are overlaid every 0.2 m/s and white contours of temperature ever 2° C.

adding ∂_y of the vertical momentum (i.e., hydrostatic balance) equation yielding

$$D_t\omega_x = \underbrace{f\partial_z u + \partial_y b}_{\text{Thermal Wind Terms}} - \partial_z v\partial_x u + \partial_x v\partial_z u - \partial_z Y, \tag{5}$$

where $\omega_x = -\partial_z v$, the material derivative $D_t = \partial_t + u\partial_x + v\partial_y + w\partial_z$, and Y is the frictional tendency of meridional momentum (e.g., due to the meridional wind stress) (Cherian et al. 2021). It may be noted that the term $\partial_y w$ is not included in the zonal vorticity ω_x to be consistent with hydrostatic dynamics of the MITgcm simulation, hence (5) is identical to the governing equation for the meridional shear $\partial_z v$ if the signs are flipped (as in Cherian et al. 2021). The zonal vorticity dynamics is approximately in thermal wind balance and the imbalance ϕ is small/weak when each of the two thermal wind terms are much larger than all other terms and about equal and opposite (5), as shown in Fig. 8. The small departures from mean thermal wind balance in Fig. 8 mainly reflect the role of the meridional wind stress and friction $\partial_z Y$ that contribute to balancing $f\partial_z u$ (off the equator) and $\partial_y b$ (on the equator) in the upper 20 m. In the zonally-symmetric, linear, and inviscid limits, the tendency of zonal vorticity $\partial_t \omega_x$ can then be approximated as

$$\partial_t \omega_x \approx f \partial_z u + \partial_y b \equiv \phi. \tag{6}$$

In (6), ϕ is the zonal vorticity tendency.

b. Derivation

The governing equation for the zonal (95°W-170°W) and time (1999-2018) averaged thermal wind imbalance $\overline{\phi}$ can be derived following the definition in (4) and applying $f\partial_z$ to the averaged equation for the zonal momentum,

$$\overline{\partial_t u} + \overline{u}\,\overline{\partial_x u} + \overline{v}\partial_y \overline{u} + \overline{w}\partial_z \overline{u} - f\overline{v} = -\frac{1}{\rho_0}\overline{\partial_x p} + \underbrace{\overline{\partial_z \left(K_m \partial_z u\right)}}_{\overline{X}_{vmix}} \underbrace{-\overline{\nabla \cdot (\mathbf{u}u)} + \overline{u}\,\overline{\partial_x u} + \overline{v}\partial_y \overline{u} + \overline{w}\partial_z \overline{u}}_{\overline{X}_{eddy}}, \tag{7}$$

where $\mathbf{u}$ is the three-component velocity vector, $\nabla\cdot$ represents the three-component divergence operator, p is the pressure and K_m is the turbulent vertical viscosity of momentum, and adding the result to ∂_y of the averaged equation for the buoyancy, given by

$$\overline{\partial_t b} + \overline{u}\,\overline{\partial_x b} + \overline{v}\partial_y \overline{b} + \overline{w}\partial_z \overline{b} \quad = \quad \overline{B}_{vmix} + \overline{B}_{eddy}. \tag{8}$$

All terms with overbars depend only on latitude and depth. The overbars are left outside of derivatives ∂_t and ∂_x, so they may represent $\overline{\partial_t u} = (u_{final} - u_{initial})/(20 \text{ years})$ for example. Explicit lateral mixing is omitted from (7) and (8), because lateral mixing is negligibly small compared to the other terms. The buoyancy tendency due to vertical mixing is approximated by

$$\overline{B}_{vmix} = g\alpha\left(\overline{\partial_z \left(K_T \left(\partial_z T + \gamma_T\right)\right)}\right) - g\beta\left(\overline{\partial_z \left(K_T \left(\partial_z S + \gamma_S\right)\right)}\right) + \overline{B}_{solar}, \tag{9}$$

and the eddy flux convergence of buoyancy is approximated by

$$\begin{aligned} \overline{B}_{eddy} = \quad & + \quad g\alpha\left(-\overline{\nabla \cdot (\mathbf{u}T)} + \overline{u}\,\overline{\partial_x T} + \overline{v}\partial_y \overline{T} + \overline{w}\partial_z \overline{T}\right) \\ & - \quad g\beta\left(-\overline{\nabla \cdot (\mathbf{u}S)} + \overline{u}\,\overline{\partial_x S} + \overline{v}\partial_y \overline{S} + \overline{w}\partial_z \overline{S}\right) \end{aligned} \tag{10}$$

where T is the potential temperature, S is the salinity, K_T is the turbulent vertical diffusivity for tracers, γ_T and γ_S are the nonlocal vertical gradients of temperature and salinity (see Large et al. 1994), and B_{solar} is the buoyancy tendency owing to penetrating solar radiation. The right hand side terms in (8) are approximate because the thermal expansion coefficient α and the haline constraction coefficient β are calculated offline using the time-mean three-dimensional temperature and salinity fields (McDougall 1987) and then averaged zonally. In addition, because the salinity budget diagnostics were not saved at runtime, the advective flux divergence of salinity $\overline{\nabla \cdot (\mathbf{u}S)}$ is calculated offline using daily three dimensional fields of $\mathbf{u}$ and S. The term in (9) associated with the vertical mixing of salinity is defined by the reconstructed advective tendency of salinity assuming steady state, that is

$$\overline{\partial_z \left(K_T \left(\partial_z S + \gamma_S \right) \right)} = \overline{\nabla \cdot (\mathbf{u}S)}. \tag{11}$$

The resulting steady state equation for $\overline{\phi}$ is given by

$$\begin{aligned}
&\overline{u}[f\partial_z(\overline{\partial_x u}) + \partial_y(\overline{\partial_x b})] + \overline{v}\partial_y\overline{\phi} + \overline{w}\partial_z\overline{\phi} \\
-\partial_y f\overline{v}\partial_z\overline{u} + f\partial_z\overline{u}\,\overline{\partial_x u} + \partial_y\overline{u}\,\overline{\partial_x b} + f\partial_z\overline{v}\partial_y\overline{u} + \partial_y\overline{b}\partial_y\overline{v} &+ f\partial_z\overline{u}\partial_z\overline{w} + \partial_y\overline{w}\partial_z\overline{b} - f^2\partial_z\overline{v} + f\overline{\partial_x b} \\
&= f\partial_z\overline{X} + \partial_y\overline{B},
\end{aligned} \tag{12}$$

where the forcing terms $\overline{X} = \overline{X}_{vmix} + \overline{X}_{eddy}$ and $\overline{B} = \overline{B}_{vmix} + \overline{B}_{eddy}$ contain the frictional and diabatic effects of both vertical mixing (vmix) and eddy flux convergences (eddy). The meridional and vertical velocities are then decomposed into two parts, $\overline{v} = \overline{v}_a + \overline{v}_g$ and $\overline{w} = \overline{w}_a + \overline{w}_g$, and (12) is reorganized so the "a" (for ageostrophic) terms are on the left side to be solved for and the "g" (for geostrophic) terms are on the right side as forcings:

$$\begin{aligned}
f(f - \partial_y\overline{u})\partial_z\overline{v}_a - \partial_y\overline{w}_a\partial_z\overline{b} - \partial_y\overline{b}\partial_y\overline{v}_a - f\partial_z\overline{u}\partial_z\overline{w}_a - \overline{v}_a\partial_y\overline{\phi} - \overline{w}_a\partial_z\overline{\phi} + \partial_y f\overline{v}_a\partial_z\overline{u} = \\
-f\partial_z\overline{X} - \partial_y\overline{B} \\
+\overline{u}[f\partial_z(\overline{\partial_x u}) + \partial_y(\overline{\partial_x b})] + \overline{v}_g\partial_y\overline{\phi} + \overline{w}_g\partial_z\overline{\phi} - \partial_y f\overline{v}_g\partial_z\overline{u} \\
+\overline{\partial_x b}\partial_y\overline{u} + f\partial_z\overline{v}_g\partial_y\overline{u} + \partial_y\overline{b}\partial_y\overline{v}_g - f\partial_z\overline{u}\partial_y\overline{v}_g \\
+\partial_y\overline{w}_g\partial_z\overline{b} - f(f\partial_z\overline{v}_g - \overline{\partial_x b}).
\end{aligned} \tag{13}$$

The flow decomposition is defined so that $\partial_y \overline{v}_a = -\partial_z \overline{w}_a$ such that this meridional circulation can be defined by a stream function $\overline{\psi}$ with $\overline{v}_a = \partial_z \overline{\psi}$ and $\overline{w}_a = -\partial_y \overline{\psi}$. Thus, $\partial_z \overline{w}_g = -\overline{\partial_x u} - \partial_y \overline{v}_g$, which has been used to simplify the right hand side of (13). We then rewrite (13) as

$$\mathcal{L}\overline{\psi} = -f\partial_z \overline{X} - \partial_y \overline{B} - 2Q \tag{14}$$

where

$$\mathcal{L} = F^2 \partial_{zz} + N^2 \partial_{yy} + 2M^2 \partial_{zy} - \partial_y \overline{\phi} \partial_z + \partial_y f \partial_z \overline{u} \partial_z + \overline{\phi} \partial_{zy} + \partial_z \overline{\phi} \partial_y, \tag{15}$$

and the last three rows of (13) are encapsulated in $-2Q$ consistent with that used in studies of midlatitude frontogenesis (Hoskins et al. 1978; Hoskins 1982; Giordani et al. 2006; Thomas et al. 2008, 2010; McWilliams 2021), where $Q \approx -\overline{\partial_x b}\partial_y \overline{u} - \partial_y \overline{v}_g \partial_y \overline{b}$ and only the first two or three terms in (15) are retained. With the exception of the last term in (13), the Q forcing reflects the disruption of thermal wind balance by geostrophic advection. We refer to (14) as the Eliassen equation or Eliassen model[1] and the operator $\mathcal{L}$ defined by (15) as the Eliassen operator, in which $F = \sqrt{f(f - \partial_y \overline{u})}$ is the effective Coriolis frequency, $M^2 = -\partial_y \overline{b} \approx f\partial_z \overline{u}$ and M is the horizontal buoyancy frequency, and $N = \sqrt{\partial_z \overline{b}}$ is the vertical buoyancy frequency. The terms in (15) are ordered by their maximum magnitude in (13) as diagnosed in the MITgcm, from largest on the left to smallest on the right.

The Eliassen equation (14) expresses a balance whereby advection of buoyancy and absolute zonal momentum by the mean meridional circulation ($\overline{\psi}$) restores the steady state thermal wind balance in opposition to the processes on the right hand side of (14) that destroy thermal wind balance. The Eliassen operator (15) reflects the stiffness of the background state to zonally-symmetric meridional and vertical parcel motions and thus tilts and stretches the circulation depending on the spatially variable effective Coriolis frequency and horizontal and vertical buoyancy frequencies (Eliassen 1951). Whitt and Thomas (2013) use parcel arguments to interpret this "stiffness" as the frequency of the associated zonally-uniform inertia-gravity waves, which depends on F, M, N and the angle of the parcel displacement (see also Hoskins 1974).

The solution and interpretation of the Eliassen model depends on choosing the decomposition of the meridional circulation, i.e. $\overline{v} = \overline{v}_g + \overline{v}_a$ and $\overline{w} = \overline{w}_g + \overline{w}_a$ that are nominally geostrophic and

[1]This equation (14) could also be referred to as a generalized omega equation (Giordani et al. 2006; Thomas et al. 2010). We refer to it as an Eliassen equation to recognize the importance of the frictional X and diabatic B forcing in this context (as in Eliassen 1951).

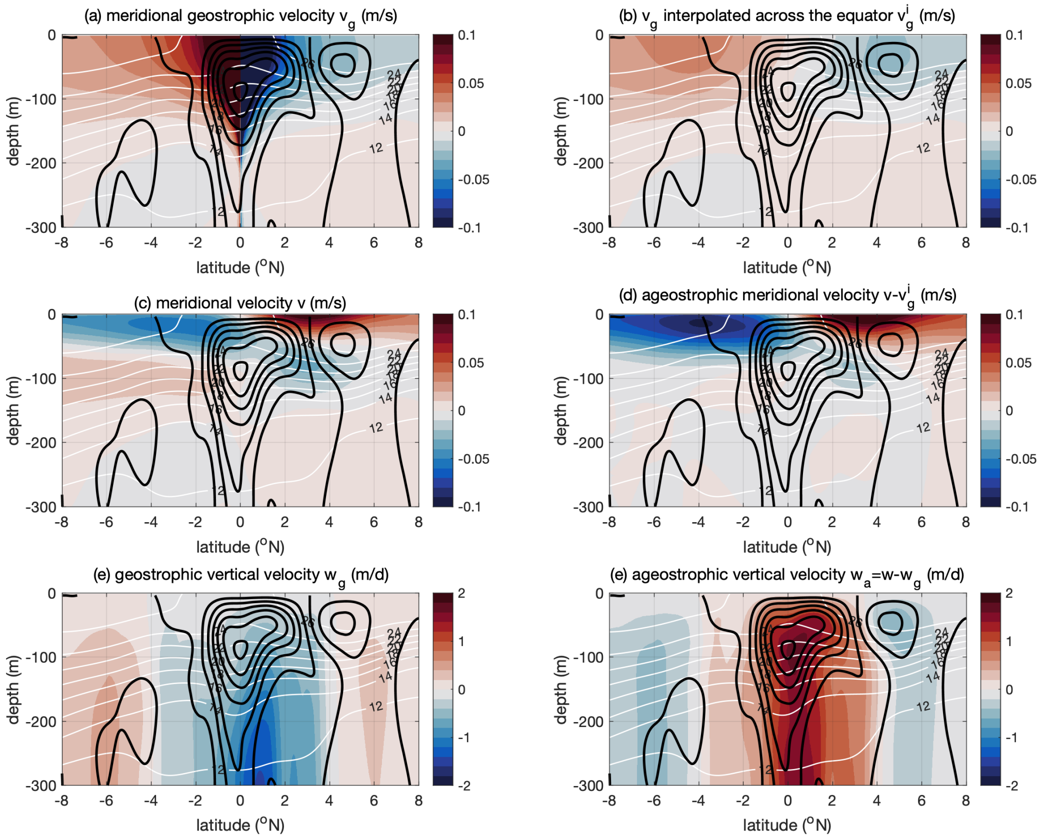

FIG. 9. Derived from MITgcm output: (a) the zonal and time mean simulated meridional geostrophic velocity $\overline{v}_g$, (b) the meridional geostrophic velocity interpolated across the equator $\overline{v}_g^i$, (c) the total meridional velocity $\overline{v}$, (d) the ageostrophic meridional velocity $\overline{v}_a = \overline{v} - \overline{v}_g^i$, the (e) geostrophic vertical velocity $\overline{w}_g$ defined by (17), and (f) the ageostrophic vertical velocity $\overline{w}_a$ defined by (18). Total vertical velocity contours of $\overline{w}$ are overlaid in black every 0.2 m/d and potential temperature $\overline{T}$ contours are in white every 2°C.

ageostrophic. However, the meridional geostrophic flow $\overline{v}_g$ is singular at the equator as well as convergent and associated with significant downwelling (Fig. 9a). To eliminate the singularity, we interpolate $\overline{v}_g$ across the equator (Lagerloef et al. 1999; Bonjean and Lagerloef 2002) by first fitting a 5th order polynomial in latitude $\overline{v}_g^p(y,z)$ to $\overline{v}_g(y,z)$ between 4° and 10° from the equator at each depth z. Then we set $\overline{v}_g^i$ to be given by:

$$\begin{aligned}
\overline{v}_g^i &= \overline{v}_g \quad |y| > 7.5^\circ, \\
\overline{v}_g^i &= \overline{v}_g^p \quad |y| < 3^\circ, \\
\overline{v}_g^i &= \left(\frac{7.5^\circ - |y|}{7.5^\circ - 3^\circ}\right)\overline{v}_g^p + \left(\frac{|y| - 3^\circ}{7.5^\circ - 3^\circ}\right)\overline{v}_g \quad 7.5^\circ \geq |y| \geq 3^\circ. \qquad (16)
\end{aligned}$$

Thus between 7.5° and 3° from the equator in both hemispheres $\overline{v}_g^i$ is a weighted average of $\overline{v}_g$ and $\overline{v}_g^p(y,z)$. To ensure that the geostrophic meridional divergence $\partial_y \overline{v}_g^i$ is smooth, $\overline{v}_g^i$ is smoothed with a 0.5° meridional moving average at each depth level. We use the resulting interpolated and smoothed geostrophic velocity $\overline{v}_g^i$ and the ageostrophic velocity that is given by $\overline{v}_a = \overline{v} - \overline{v}_g^i$ (Figs. 9b and d). The ageostrophic meridional velocity $\overline{v}_a$ has a similar yet stronger pattern as $\overline{v}$ above 50 m depth, because $\overline{v}_g$ acts to compensate the Ekman transport (c.f., Figs. 9c-d). On the other hand, $\overline{v}_a$ is similar to but much weaker than $\overline{v}$ between 50-150 m depth, where $\overline{v}$ is dominated by the equatorward geostrophic flow (c.f., Figs. 9c and d).

Using $\overline{v}_g^i$ to define $\overline{v}_g$ in the Eliassen model allows the decomposition of the vertical velocity $\overline{w} = \overline{w}_g + \overline{w}_a$, such that

$$\overline{w}_g(y,z) = \int_z^0 \left(\partial_y \overline{v}_g^i + \overline{\partial_x u}\right) dz, \qquad (17)$$

and

$$\overline{w}_a(y,z) = \int_z^0 \partial_y \overline{v}_a dz = \overline{w} - \overline{w}_g. \qquad (18)$$

The integrals are computed using trapezoidal numerical integration. We find that $\overline{w}_g$ and $\overline{w}_a$ generally tend to compensate each other (c.f., Figs. 9e-f; see also Section 2.c and Fig. 2). Near the surface (e.g., at 50 m), $\overline{w}_a$ overwhelms $\overline{w}_g$ and the pattern of $\overline{w}$ is similar to that of $\overline{w}_a$, while $\overline{w}_g$ and $\overline{w}_a$ are more nearly equal and opposite at deeper depths (e.g., below 200 m) where net upwelling $\overline{w}$ tends to be much weaker than $\overline{w}_a$.

The streamfunction of the Eliassen circulation $\overline{\psi}$ can be obtained by inverting the Eliassen operator $\mathcal{L}$ to solve the Eliassen equation (14) when both the operator $\mathcal{L}$ and the right-hand-side forcing terms are known. Although the forcing terms cannot readily be calculated from observations, they can be determined using the MITgcm budget diagnostics. To decompose the contribution of the various process drivers to $\overline{\psi}$ and $\overline{w}_a$, we solve the Eliassen equation (14) multiple

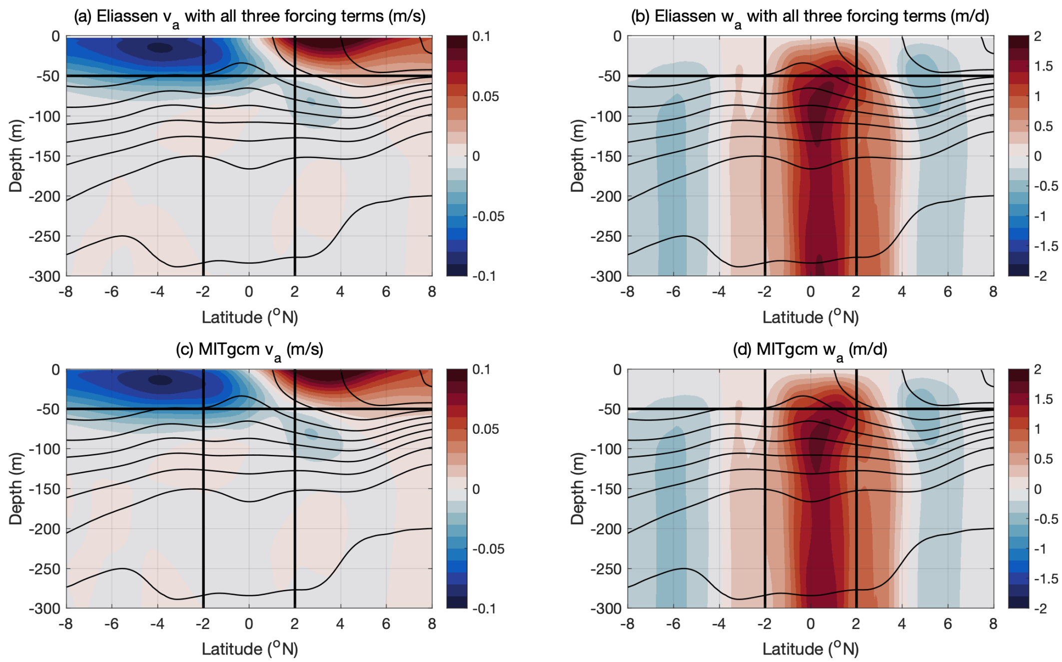

FIG. 10. The meridional and vertical ageostrophic velocities $\overline{v}_a$ (a,c) and $\overline{w}_a$ (b,d) from the Eliassen model (14) with all three forcings (top: a,b) and the MITgcm (bottom: c,d). The potential density $\overline{\rho}$ is contoured in black every 0.5 kg/m^3. Thick horizontal and vertical lines at 50 m depth and 2° respectively simply help provide spatial points of reference (as in Fig. 3a).

times, once for each process-separated driver defined above [$\overline{X}_{vmix}$ given by (7), $\overline{B}_{vmix}$ given by (9), $\overline{X}_{eddy}$ given by (7), $\overline{B}_{eddy}$ given by (10), and $-2Q$ given by (13) with $\overline{v}_g$ given by $\overline{v}_g^i$ defined by (16) and $\overline{w}_g$ defined by (17)]. Since (14) is linear, the process-separated stream functions add to give the process-combined stream function. The result is quantitative separation and attribution of the meridional circulation $\overline{\psi}$ and upwelling $\overline{w}_a$ due to eddy advection, vertical mixing, and Q forcing.

c. Numerical solution of the Eliassen model

Solutions to the Eliassen model (14) are obtained numerically following the procedure in Whitt and Thomas (2013). Discrete forms of the operator $\mathcal{L}$ and the right hand side of Equation (14) are constructed on a 200-by-200 point depth-latitude Eliassen model grid. The horizontal Eliassen grid evenly spans 10°S to 10°N with 11 km resolution, and the vertical Eliassen grid evenly spans the top 600 m depth with 3 m resolution. Boundary conditions on $\overline{\psi}$ are incorporated into 4th-order central finite difference discretizations of the first and second derivatives in both y and z. These discrete derivative operators are then used to construct the discrete version of $\mathcal{L}$. At the surface, $\overline{\psi} = \partial_y \overline{\psi} = \overline{w} = 0$, and at the bottom $\partial_z \overline{\psi} = \overline{v} = 0$. Likewise $\partial_y \overline{\psi} = \overline{w} = 0$ at the meridional boundaries. A constant vertical eddy viscosity 10^{-4} m^2/s is added to prevent the appearance of small overturning cells in the top 50 m within a degree of the equator. Sensitivity tests for $\overline{\psi}$ showed that this introduced viscosity does not have a large impact on the solution.

The inputs to the Eliassen model, including $\overline{u}(y,z)$ and $\overline{b}(y,z)$ that are used in $\mathcal{L}$ and the right hand side drivers $\overline{X}$ and $\overline{B}$ and Q, are constructed from the MITgcm output and interpolated to the Eliassen grid. In the construction and evaluation of the Eliassen model in sections 3-4, the zonal averages always exclude longitudes where there is at least one land point in a 40-km-wide meridional strip around that longitude, which eliminates about 11% (880 km) of the zonal extent of the domain due to the Line Islands and Marquesas Islands. Before interpolating to the Eliassen grid, the inputs from the MITgcm are also smoothed with a 0.5° meridional moving average at each depth to suppress residual small-scale variability.

d. Evaluation

With all three right-hand-side forcings included in (14), the solution of the Eliassen model almost exactly reproduces the ageostrophic meridional circulation in the MITgcm (c.f. Figs. 10a-b with Figs. 10c-d, and see Fig. 11). In addition, the meridional asymmetry of $\overline{w}_a$ largely explains the meridional asymmetry in $\overline{w}$ at 50 m depth (Fig. 11; see also Fig. 9e-f). Thus, we proceed to use the Eliassen model to decompose the processes responsible for the meridional asymmetry in $\overline{w}_{50}$ in the MITgcm.

4. Decomposing the meridional circulation and upwelling by process using the Eliassen model

Here, we compare the solutions for $\overline{\psi}$ and $\overline{w}_a$ from the Eliassen model (14) in the top 300 m separately for each driver. Before proceeding, we note that the spatial variability of $\overline{b}(y,z)$ and $\overline{u}(y,z)$ inherent in $\mathcal{L}$ contributes to the spatial structure of the meridional circulation and upwelling in the Eliassen model. However, by solving the Eliassen model with a simplified operator $\mathcal{L}$ defined by the horizontally averaged buoyancy profile $\langle \overline{b} \rangle^y(z)$ with $\overline{u} = \overline{\phi} = 0$ (such that $F^2 = f^2$, $M^2 = 0$ and

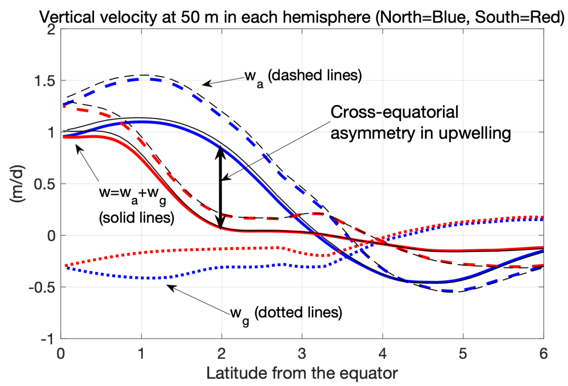

FIG. 11. The Eliassen model (thin black lines) almost exactly reproduces the meridional structure of the vertical velocity at 50 m depth in both hemispheres of the MITgcm simulation (thick lines; north=blue, south=red). The Eliassen solution of (14) yields the ageostrophic vertical velocity $\overline{w}_a$ (dashed lines) defined by (18). The geostrophic vertical velocity $\overline{w}_g$ (thick dotted lines) defined by (17) has been added to the ageostrophic velocity $\overline{w}_a$ obtained from the Eliassen model to obtain $\overline{w} = \overline{w}_g + \overline{w}_a$ (thin solid lines) for comparison with $\overline{w}$ from the MITgcm (thick solid lines), which is also plotted in Fig. 3a-b.

$N^2 = \langle N^2 \rangle^y$), we found that the meridional asymmetry of the Eliassen w at 50 m with the simplified $\mathcal{L}$ (not shown) is qualitatively similar to the solution obtained with the full $\mathcal{L}$ (shown in Fig. 10)[2]. Conversely, by solving the Eliassen model with the full $\mathcal{L}$ and with simplified meridionally averaged forcing terms (e.g., as shown in the next section), we found that the meridional structure of these forcing terms is critical to the meridional asymmetry in upwelling at 50 m. Hence, we focus on separating and quantifying the sensitivity of the Eliassen solutions to the right-hand side forcing terms. In addition, preliminary analysis of the Eliassen model in two sectors (168°W-132°W and 132°W-97°W; not shown) suggests that zonal variations, including the shift in peak upwelling at 50 m from about 1°N west of 130°W to about 0.5°S east of 130°W, are captured by the Eliassen model. However, the meridional asymmetry in upwelling that peaks near 2° is qualitatively similar in both sectors (magenta dots in Fig. 3c) and arises for similar reasons in both sectors (not shown). Hence, we focus on recovering the zonal mean $\overline{w}$ over the entire MITgcm domain (95°W-170°W) using the Eliassen model leaving an analysis of the processes driving zonal variations in the meridional structure of upwelling to future work.

---

[2]However, the regularity of the Eliassen solution relies on the fact that $N^2 > 0$ everywhere. Regularity issues also arise where the principal part of the Eliassen operator becomes hyperbolic instead of elliptic, or where the potential vorticity of the mean state defined by $\overline{u}$ and $\overline{b}$ takes the opposite sign of f such that the flow is symmetrically unstable (Hoskins 1974; Whitt and Thomas 2013). As discussed in Section 3.c, the weak vertical viscosity regularizes minor issues of this nature that arise at just a few grid cells.

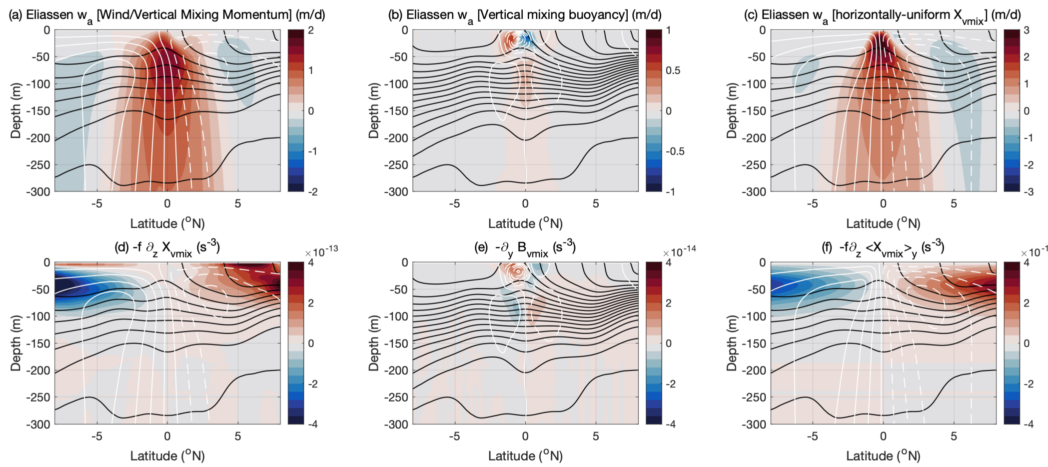

FIG. 12. Solutions of the Eliassen model (14) for the drivers associated with vertical mixing $\overline{X}_{vmix}$ and $\overline{B}_{vmix}$. The ageostrophic vertical velocity $\overline{w}_a$ is colored in the top panels and the corresponding thermal wind imbalance driver is colored in the bottom panels. Note the different color scales. (a) reflects the upwelling driven by the zonal wind and vertical mixing of zonal momentum shown in (d), while (b) reflects the upwelling driven by the vertical mixing of buoyancy shown in (e). Mean potential density $\overline{\rho}$ is contoured every 0.5 kg/m^3 in black, and the stream function of the Eliassen circulation $\overline{\psi}$ is contoured in white every 1 m^2/s in (a), (c), (d) and (f) and 0.1 m^2/s in (b) and (e). The results in (c) are similar to (a) except that the driver $\overline{X}_{vmix}$ is set to its horizontally uniform mean to test the sensitivity to its meridional structure. Meridional structure in $f\partial_z\langle\overline{X}_{vmix}\rangle^y$ in (f) is due entirely to meridional structure in the Coriolis frequency f.

a. Turbulent vertical mixing

Equatorial upwelling is mainly driven by zonal wind stress that accelerates the zonal flow via vertical mixing $\overline{X}_{vmix}$ resulting in meridionally divergent Ekman transport centered on the equator (Fig. 12a). Thus, the Eliassen model driven by $\overline{X}_{vmix}$ alone (Fig. 12d) yields a solution for $\overline{w}_a$ (Fig. 12a) that captures many features of the full ageostrophic vertical velocity $\overline{w}_a$ (c.f. Figs. 10b,d). For example, this wind-driven part of $\overline{w}_a$ peaks near the equator between 50-100 m depth with magnitude of 1.5-2 m/d. The width of this wind-driven upwelling spans roughly 4°S-4°N below 100 m but is strongest within about 2° of the equator. In addition, this wind-driven $\overline{w}_a$ has lobes of downwelling poleward of the upwelling with similar magnitude and spatial structure as the full $\overline{w}_a$ shown in Figs. 10b,d. However, the acceleration of the zonal flow due to the wind and vertical mixing $\overline{X}_{vmix}$ is insufficient to drive the meridional asymmetry in the full $\overline{w}_a$ and $\overline{w}$ at 50 m (c.f. Figs. 10b,d and 11 to Fig. 12a).

Using the Eliassen model, we can explore the sensitivity of the wind-driven circulation and upwelling to the spatial structure of the vertical mixing of momentum by varying the structure of $\overline{X}_{vmix}$. For example, we meridionally average $\langle\overline{X}_{vmix}\rangle^y$ within 8° and replace $\overline{X}_{vmix}$ in the Eliassen model, which becomes

$$\mathcal{L}\overline{\psi} = -f\partial_z\langle\overline{X}\rangle^y. \tag{19}$$

Peak upwelling is notably shallower, more narrowly confined to the equator, and stronger if the mixing is independent of latitude (c.f. Figs. 12c,f to Figs. 12a,d). The strong shallow upwelling on the equator above 50 m depth (Fig. 12c) and the meridional divergence at 15 m (not shown) under horizontally uniform mixing is more similar to the studies of Poulain (1993) and Karnauskas (2025) that use drifter data to calculate strong meridional divergence at 15 m on the equator. Karnauskas (2025) shows that strong shallow divergence tends to be missing from coarser resolution simulations and becomes more realistic as the resolution is refined. However, the MITgcm simulation has finer horizontal and vertical resolution than any simulation considered by Karnauskas (2025), yet it does not exhibit strong divergence at 15 m on the equator as shown in analysis of drifters (see also Fig. A5b). These results suggest that the surface meridional divergence and the shallow upwelling on the equator are quite sensitive to the parameterized vertical structure of vertical mixing near the equator, which depends on grid resolution and the vertical mixing parameterization.

The ageostrophic upwelling below 50 m is less sensitive to the meridional structure of vertical mixing of momentum (c.f. Figs. 12c,f to Figs. 12a,d). This suggests that meridional variations in the zonal wind stress magnitude or vertical mixing of momentum due to ocean vertical shear and stratification variations, e.g. due to the EUC or tropical instability wave activity, are less important than the meridional structure of f in setting the meridional structure of the upwelling below 50 m in Fig. 12a. In addition, the meridional asymmetry in upwelling at 50 m off the equator is relatively insensitive to the meridional structure of $\overline{X}_{vmix}$.

Another possible cause of the meridional asymmetry in upwelling is buoyancy tendencies owing to vertical mixing $\overline{B}_{vmix}$ that also destroy thermal wind balance and hence induce a vertical circulation $\overline{w}_a$ (Figs. 12b,e). But the vertical motion $\overline{w}_a$ due to $\overline{B}_{vmix}$ is considerably weaker and more spatially limited near the equator than that associated with the wind and the vertical mixing

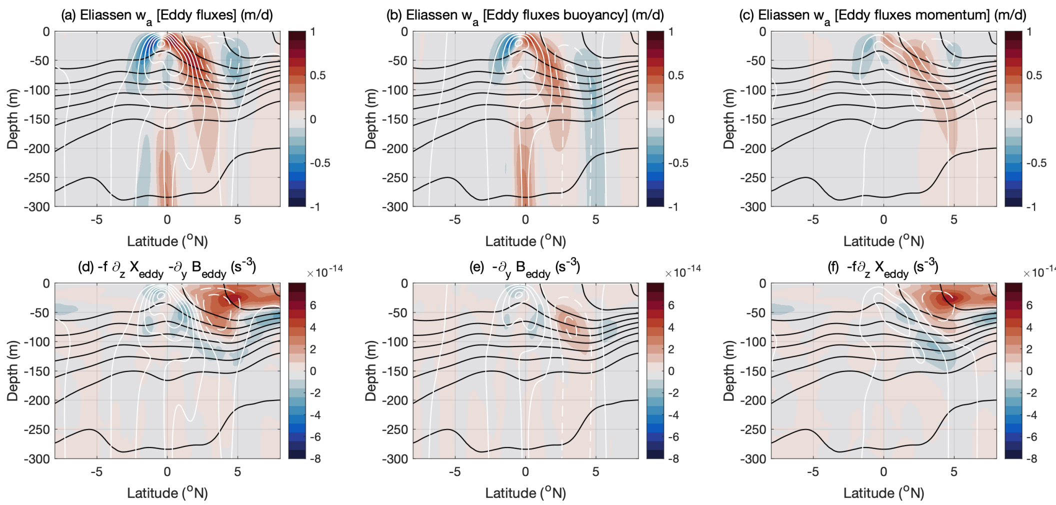

FIG. 13. As in Fig. 12, but solutions of the Eliassen model (14) for the drivers associated with eddy advection $\overline{X}_{eddy}$ and $\overline{B}_{eddy}$: (a) reflects the response to eddy advection of zonal momentum $\overline{X}_{eddy}$ and buoyancy $\overline{B}_{eddy}$ combined as shown in (d), (b) reflects the response to $\overline{B}_{eddy}$ only as shown in (e), and (c) reflects the response to $\overline{X}_{eddy}$ only as shown in (f). The stream functions $\overline{\psi}$ are contoured every 0.2 m^2/s in white in all panels. Note the different color scales relative to Fig. 12.

of momentum $\overline{X}_{vmix}$ (c.f. Figs. 12b,e to Figs. 12a,d). The vertical velocity $\overline{w}_a$ from $\overline{B}_{vmix}$ has very little impact on upwelling at 50 m (Fig. 12b).

Thus, the combined driving by turbulent vertical mixing expressed in $\overline{X}_{vmix}$ and $\overline{B}_{vmix}$ is not sufficient to drive the meridional asymmetry in $\overline{w}_a$ at 50 m that is simulated by the MITgcm and captured by the full Eliassen model.

b. Eddy advection

The eddy-driven part of the circulation $\overline{\psi}$ (forced by $\overline{X}_{eddy}$ and $\overline{B}_{eddy}$) is dominated by two counter-rotating meridional cells in the top 100 m (Fig. 13a). A counterclockwise cell about 4° wide is centered on the equator, and a slightly narrower and weaker clockwise cell is centered near 4°N. The associated vertical velocity $\overline{w}_a$ has a tripole structure with a strong upwelling of about +0.7 m/d at 2°N and 50 m depth between the two cells compensated by weaker downwelling lobes near 2°S and 5°N on the edges of the cells. On the equator, the eddy driven $\overline{w}_a$ at 50 m is an order of magnitude weaker than the wind-driven upwelling (consistent with the conclusion of Bryden

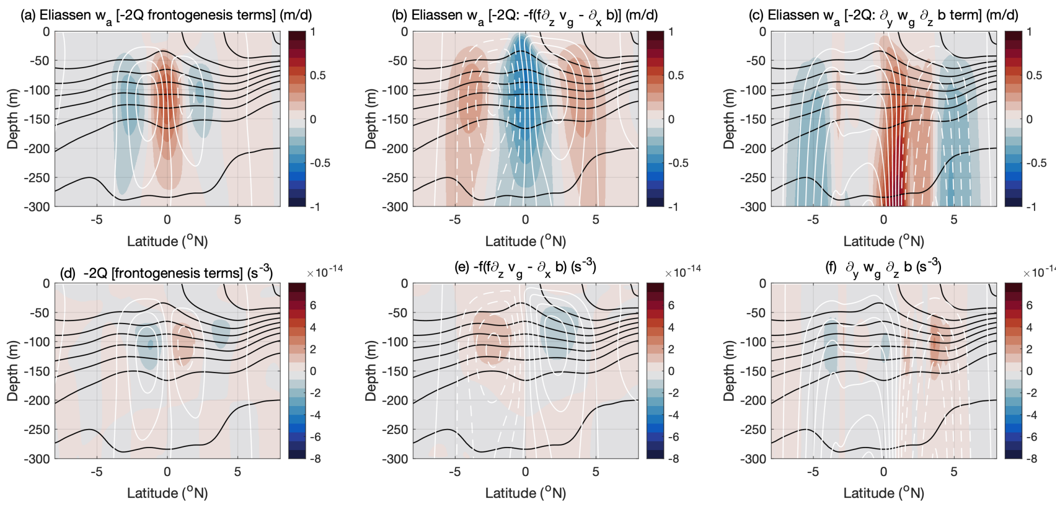

FIG. 14. As in Fig. 13, but solutions of the Eliassen model (14) for the dominant terms associated with the Q forcing $-2Q$: (a) reflects the response to the frontogenesis terms shown in (d), which are on the 4th line of (13) and dominated by $\partial_y \overline{u} \overline{\partial_x b}$. (b) reflects the response to rotation of meridional thermal wind imbalance into zonal thermal wind imbalance $-f(f\partial_z \overline{v}_g^i - \overline{\partial_x b})$ shown in (e). (c) reflects the response to differential vertical advection of the stratification $\partial_y \overline{w}_g \partial_z \overline{b}$ shown in (f).

and Brady 1989). Thus, the eddy-driven circulation is important for the meridional asymmetry of off-equatorial upwelling at 50 m, although eddy activity contributes little to upwelling right on the equator.

c. Q forcing

The Q-forcing contains a daunting collection of terms, including the third, fourth and fifth lines of (13), but many of the terms are weak and have little impact on the vertical circulation in the MITgcm. For example, all of the terms on the third line of (13) arising from the geostrophic advection of thermal wind imbalance and the meridional gradient of the Coriolis frequency $\partial_y f$ produce a weak vertical circulation (not shown), so we do not consider them any further.

The terms responsible for frontogenesis in midlatitudes on the fourth line of (13) produce little vertical motion in the equatorial Pacific except for one term: $\partial_y \overline{u} \overline{\partial_x b}$. This term drives a significant equatorial upwelling because the strong meridional shear of the zonal currents and particularly the EUC tilt the zonal buoyancy gradient in the equatorial thermocline into a meridional buoyancy gradient (Fig. 14d). The resulting thermal wind imbalance tendency drives a tripolar vertical velocity $\overline{w}_a$ near the depth of the undercurrent core with an upwelling of about 0.5 m/d on the equator flanked by downwellings about half as fast near ±2.5° (Fig. 14a). However, the ageostrophic vertical velocity $\overline{w}_a$ due to the frontogenesis terms is relatively symmetric about the equator and relatively weak near 50 m depth.

The last two terms of the Q forcing on the fifth line of (13) are the strongest, and these terms are unique to the equatorial application where $\overline{v}_g$ is not geostrophic everywhere and $\overline{w}_g$ is not zero everywhere. One of these two terms arises from the rotation of meridional thermal wind imbalance $(f\partial_z\overline{v}_g - \overline{\partial_x b})$ into zonal thermal wind imbalance $\overline{\phi}$ at a rate $f(f\partial_z\overline{v}_g - \overline{\partial_x b})$. This rotation depends on f and is thus fairly symmetric about the equator (Fig. 14e) and yields a fairly symmetric tripolar pattern in $\overline{w}_a$ with downwelling on the equator of about 0.5 m/d and upwelling about half as strong near ±4° (Fig. 14b). This rotation can be understood as compensating a small portion of the upwelling driven by the wind forcing $f\partial_z\overline{X}_{vmix}$ (c.f. Figs. 12a and 14b), which is balanced more by $f\overline{\partial_x b}$ than by $f^2\partial_z\overline{v}_a$ near the equator (as is well known in the context of zonal momentum budget; see e.g. Qiao and Weisberg 1997).

The other of the two Q terms on the fifth row of (13) is $\partial_y\overline{w}_g\partial_z\overline{b}$ (Fig. 14f), which reflects the generation of $\partial_y\overline{b}$ and thermal wind imbalance $\overline{\phi}$ by differential vertical advection of N^2 by $\overline{w}_g$ (Fig. 9e). Differential vertical advection of N^2 by $\overline{w}_g$ is an important source of meridional asymmetry in $\overline{w}_a$ (Fig. 14c), which exhibits a tripolar pattern with upwelling between the equator and 4° N and weaker downwellings near 5° S and 5° N. However, in contrast to the eddy-driven vertical circulation, which is largely confined to the top 100 m and peaks near 50 m (Fig. 13a), the part of $\overline{w}_a$ that balances differential vertical advection by $\overline{w}_g$ is fairly weak in the top 50 m and strengthens from 50-150 m. Below 150 m, this Q-driven $\overline{w}_a$ compensates much of the asymmetry in $\overline{w}_g$ and acts to return $\overline{w}$ to a more symmetric meridional profile (Fig. 9e-f).

d. Causes of meridional asymmetry in upwelling

The asymmetry in $\overline{w}$ at 50 m of almost 1 m/d (northern hemisphere minus southern hemisphere) 1°-2° from the equator is attributable primarily to the ageostrophic component $\overline{w}_a$ (Fig. 11) and specifically the eddy-driven part of $\overline{w}_a$ (Fig. 15). Wind forcing and vertical mixing of zonal momentum are the dominant drivers of equatorial upwelling, but they are not responsible for

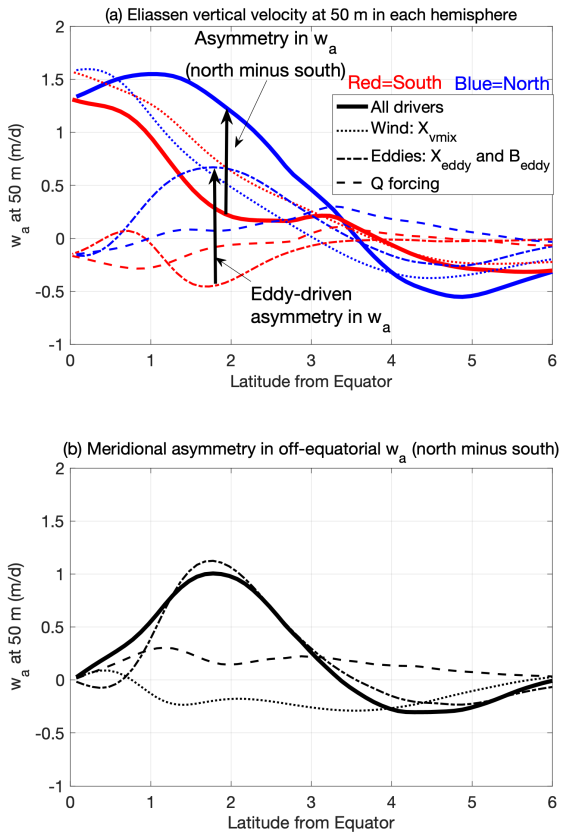

Fig. 15. A comparison between the Eliassen models of $\overline{w}_a$ at 50 m depth forced by all drivers (solid lines), by wind mixing only (i.e., by $\overline{X}_{vmix}$; dotted lines), by eddy fluxes only (i.e., by $\overline{X}_{eddy}$ and $\overline{B}_{eddy}$; dash-dotted lines), and by Q forcing only (dashed lines) in each hemisphere as in Fig. 11. The top panel (a) compares $\overline{w}_a$ while the bottom panel compares the meridional asymmetries in off-equatorial $\overline{w}_a$ (northern hemisphere minus southern hemisphere).

the meridional asymmetry in $\overline{w}$ (Fig. 15). The Q forcing (13) is responsible for significant meridional asymmetry in the ageostrophic vertical velocity $\overline{w}_a$ below 100 m depth (Fig. 14c), but this component of $\overline{w}_a$ is associated with little asymmetry in $\overline{w}$ (it mainly compensates $\overline{w}_g$). Where asymmetry in $\overline{w}$ is prominent at 50 m depth, the asymmetry in $\overline{w}_a$ attributable to the Q forcing is a modest 0.1-0.2 m/d compared to the roughly 1 m/d due to the eddy terms $\overline{X}_{eddy}$ and $\overline{B}_{eddy}$ that dominate (Fig. 15b).

5. Conclusions and Discussion of Future Research Priorities

We have shown that high-resolution ocean general circulation models of the cold tongue in the east-central equatorial Pacific simulate a previously-unknown northward-shifted upwelling core above the upwelling associated with the tilted thermocline and EUC that is centered on the equator (Deppenmeier et al. 2021). Upwelling at 50 m peaks at about 1°N (Fig. 3a-c), and asymmetry peaks at about 2° where the upwelling is almost 1 m/d in the northern hemisphere but zero in the southern hemisphere (Fig. 3a-c). Although a northward-shifted upwelling core appears in multiple eddy-resolving regional and global ocean models, the best observational estimates from surface drifter data show that the maximum of the zonal mean meridional divergence (and presumably maximum upwelling) is on the equator (Karnauskas 2025; Poulain 1993). Nevertheless, the simulated meridional asymmetry in zonal mean upwelling (here defined by the cross-equatorial difference in vertical velocity at each latitude) is mirrored by the observed asymmetry in meridional divergence at 15 m from drifters (Fig. 3b). This suggests the meridional asymmetry in off-equatorial upwelling at 50 m is a feature of the real ocean (section 2.d; Fig. 3b) even if maximum zonal-mean upwelling is on the equator when averaged from 95°W-170°W.

Unlike in the far east where southerly cross-equatorial winds might contribute to the shallow maximum in upwelling south of the equator (white dots in Fig. 3c) (McPhaden et al. 2008; Mitchell and Wallace 1992; Philander and Pacanowski 1981) or the stronger upwelling at 2°N versus 2°S (magenta dots in Fig. 3c), the zonal winds of the central Pacific are an unlikely cause of the northward shift in upwelling there. Motivated by the strongly-asymmetric tropical instability waves that have a larger impact north of the equator, we examine how the vigorous TIW eddy activity might induce the otherwise hard-to-explain meridionally asymmetric upwelling cell.

To isolate the drivers of the climatological (1999-2018 mean) upper-ocean equatorial circulation in a realistic high-resolution regional ocean simulation in the MITgcm, we use an Eliassen model of the zonal mean ageostrophic meridional circulation, appropriate for the long zonal scales of the east-central equatorial Pacific. The Eliassen model (section 3) describes the drivers of the zonal vorticity tendency and allows a linear separation of the frictional (e.g., due to wind stress), diabatic (e.g., due to surface heat flux), eddy advective flux-driven, and mean/geostrophic advection-driven vertical velocity terms. We show that the Eliassen model driven by all of these terms almost exactly reproduces the structure of the ageostrophic zonal mean meridional circulation in the

MITgcm (Figs. 10-11). The zonal wind stress and associated vertical mixing of zonal momentum accounts for the familiar centered upwelling, duplicating that part of the MITgcm solution, but the MITgcm's meridionally asymmetric w near 50 m is due to the eddy advection of zonal momentum and buoyancy that are presumably dominated by the TIW (Fig. 15). The eddy-driven mean meridional circulation is composed of two counter-rotating cells in the upper 100 m centered at the equator and 4°N that generate a peak upwelling of about 0.7 m/d in between at 2°N (Fig. 13a), where upwelling is most asymmetric across the equator. These results strengthen previous modeling studies suggesting that the mean meridional overturning circulation in the cold tongue is significantly impacted by eddy activity (McWilliams and Danabasoglu 2002; Hazeleger et al. 2001; Richards et al. 2009; Perez et al. 2010; Maillard et al. 2022).

We have also used the MITgcm to show that the meridional structure of upwelling at 50 m is modulated zonally (Fig. 3c-d), seasonally (Figs. 4-5), and interannually as part of ENSO variability (Figs. 6-7). Future application of the Eliassen model in different zonal sectors, composite seasons or ENSO phases might explain the zonal shift in maximum upwelling at 50 m from the Northern hemisphere to the Southern Hemisphere near 130°W and/or the shift in peak upwelling back to the equator and reduction in meridional asymmetry during boreal spring (Fig. 4) and El Niño (Fig. 7) in conjunction with reductions in eddy activity.

Future model intercomparisons (e.g., Karnauskas 2025) or sensitivity studies with different resolutions and subgrid scale parameterizations might help clarify the sensitivity of asymmetric eddy-driven upwelling to model formulation and possibly lead to model improvements. Future work might also quantify the broader significance of the asymmetry in upwelling identified here, e.g. for regional air-sea interaction, global climate dynamics, biogeochemistry. Finally, further data collection is needed to properly evaluate and improve the globally significant Equatorial Pacific upwelling in high resolution ocean and climate simulations.

While the observed zonal (95°W-170°W) and time mean meridional divergence at 15 m depth exhibits a similar off-equatorial meridional asymmetry as the simulated upwelling at 50 m (Fig. 3b), many of the simulated features of the divergence and upwelling have not yet been observed. An array of 13 platforms measuring vertical profiles of horizontal velocity, temperature and salinity, e.g. moorings or autonomous vehicles, spaced about every 0.5° meridionally and spanning ±3° would be sufficient to quantify the asymmetry of off-equatorial upwelling and test for the existence of the off-equatorial peak in upwelling north of the equator in the central Pacific or south of the equator in the east Pacific if sustained for a few years. Observing the zonal, seasonal and interannual variations of divergence might be possible with many repeated maps of ocean surface velocity over a few years from remote sensing, from which zonal and time averages can be combined to extract the larger-scale and lower-frequency signals from the vigorous intraseasonal variability.

Acknowledgments. DBW's time conducting the analysis and writing the paper was supported by NASA's SWOT science team (437949.02.09.01.20) and NASA's Modeling Analysis and Prediction Program (510937.05.01.01.18 and 281945.02.04.04.78). The work is also made possible by support from the NOAA Climate Variability and Predictability Program (NA18OAR4310408, NA22OAR4310595, NA22OAR4310596). We would also like to acknowledge high-performance computing support from the NASA High-End Computing (HEC) Program through the NASA Advanced Supercomputing (NAS) Division at Ames Research Center as well as Cheyenne (doi:10.5065/D6RX99HX) provided by NCARs Computational and Information Systems Laboratory, sponsored by the National Science Foundation.This material is based upon work supported by the National Center for Atmospheric Research (NCAR), which is a major facility sponsored by the NSF under Cooperative Agreement 1852977. DBW acknowledges Scott Bachman and Deepak Cherian for setting up and running the MITgcm simulation and Santha Akella and Dimitris Menemenlis for numerous helpful scientific discussions and fruitful collaboration on funding acquisition. Constructive reviews by Kris Karnauskas and an anonymous reviewer are acknowledged.

Data availability statement. The code necessary for generating the figures in the paper is published at https://github.com/danielwhitt/Eliassen-Equator/ and will be archived in a permanent location with doi upon acceptance. The data necessary for generating the figures in this paper is archived publicly at https://doi.org/10.5281/zenodo.17315962

APPENDIX

Observational evaluation of the simulation

This section compares the numerical simulation to observations. In considering these comparisons between the simulation and observations, it is necessary to keep in mind the caveat that both the simulated and observed "climatologies" are often not based on the same time periods, and both the simulation (20 years) and the observations span periods of time that are in most cases too short to fully average out the effects of internal climate variability. This caveat is particularly important for the comparisons to shipboard ADCP observations, which are derived from almost completely disjoint time periods. Nevertheless, we conclude that the qualitative and quantitative similarity between the simulation and observations indicate that both the simulation and observations express the true climatological circulation and hydrography to a first approximation, and the simulation likely captures the dominant physics of the climatological circulation.

A1. Mean hydrography

A comparison between the simulation and some available observations indicate that the simulation yields reasonably realistic hydrography. The meridional and vertical structure of the time and zonal mean temperature, salinity, and potential density are all similar to the analogous estimates from the 2004-2018 Argo climatology of Roemmich and Gilson (2009) (Fig. A1), as is the zonal difference in dynamic height, which defines the mean meridional geostrophic flow (Fig. A2).

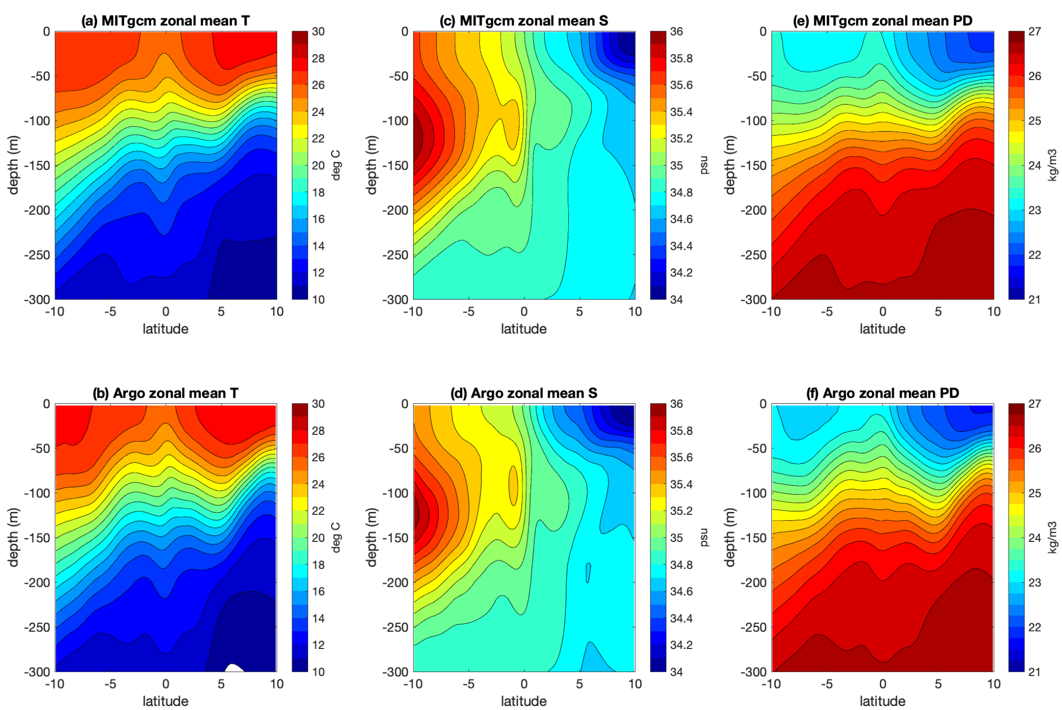

Fig. A1. The climatological zonal mean potential temperature (a)-(b), salinity (c)-(d), and potential density (e)-(f) between 168°W-97°W in the MITgcm simulation (top) are similar to the 1/6° resolution 2004-2018 Argo observational climatology of Roemmich and Gilson (2009) (bottom).

A2. Mean zonal velocity

Like the hydrography, the simulated and observed zonal mean zonal velocity u is also reasonably realistic (Figs. A3-A4). Here, the simulation is compared with three observational estimates. First, u is estimated from direct measurements of the zonal currents from shipboard ADCPs during several occupations of sections along six longitudes from 95°W-170°W in the 1990s (Johnson et al. 2002). The zonal means u are calculated by zonally averaging a cubic polynomial fit to the 6 climatological sections from 170°W through 95°W at each depth and latitude. Although direct, the shipboard ADCP observations are uncertain due to the lack of data shallower than 30 m and the relatively limited number of sections collected. Hence, u is also estimated geostrophically using the smoothed dynamic heights obtained by fitting cubic polynomials in longitude to the dynamic heights referenced to 500 m depth from the 1/6°-resolution Argo climatology of Roemmich and Gilson (2009) (Fig. A2). The resulting zonal geostrophic velocities are thought to be reasonable to about 1° latitude (Meinen and McPhaden 2001), but we found zonal velocities more consistent with direct drifter-based estimates at 15 m (Fig. A4a) if geostrophic estimates were excluded within 1.25° of the equator rather than within only 1.0°. To estimate u at latitudes equatorward of 1.25°, the moored ADCP data at 110°, 140°, and 170°W on the monthly equatorial TAO moorings (McPhaden et al. 2010) are averaged over all available times to obtain climatological vertical profiles of u from 30 to 275 m depth. The three profiles are extended to all longitudes by a quadratic polynomial fit and applied uniformly within 0.5° of the equator, leaving the geostrophic estimates at latitudes poleward of 1.25° and a gap between 0.5 and 1.25°. Finally, a sixth order polynomial is fit to the combined zonal velocity from 3°S-3°N at depths where the geostrophic and TAO ADCP data are available (and a third order polynomial is fit at depths where only the geostrophic velocities are available). This polynomial is used exclusively within 1.25° of the equator, and the polynomial contribution linearly decays from 100% at 1.25° to 0% (i.e., 100% geostrophic u) at 3°. The resulting three-dimensional mapped zonal velocity matches the TAO ADCP profiles well at the mooring locations and exhibit generally realistic structure, even in the upper 30 m where TAO data are not available (Fig. A3-A4).

The comparisons with the gcm show that the major zonal currents are all present and fairly realistic in the simulation. Notably, both the depth and speed of the Equatorial Undercurrent (EUC) are quite realistic. All the other main currents are represented, including the North Equatorial

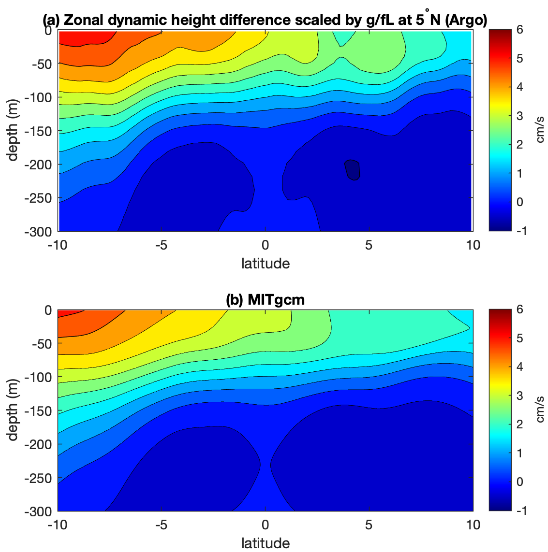

FIG. A2. The zonal difference in the dynamic height (168°W minus 97°W) referenced to 500 m depth and normalized to a meridional geostrophic velocity scale in both the 1/6° 2004-2018 Argo climatology of Roemmich and Gilson (2009) (a) and the MITgcm simulation (b). The normalization involves multiplying by a constant $g/fL = 0.1$, where $g = 9.81$ m/s^2 is the acceleration due to gravity, $f = 1.27 \times 10^{-5}$ s^{-1} is the Coriolis frequency at 5°N and, and $L = 7860$ km is the zonal length of the domain at 5°N. The dynamic heights on each end are zonally averaged in 5° windows from 163-168°W and 97-102°W, and the resulting dynamic height differences are rescaled to account for the reduction in zonal distance due to the windowed averaging.

Counter Current (NECC) in the upper 100 m at about 7°N and the Tsuchya jets: the Northern Subsurface Countercurrent (NSCC) centered at about 200 m and 4°N and the two-branched Southern Subsurface Countercurrent (SSCC) apparent between 4-8°S and 150-300 m depth. The South Equatorial Current (SEC) exhibits a realistic spatial pattern north and south of the equator but is notably weaker than in the observations. A qualitatively similar conclusion regarding the weakness of the SEC can be derived from a comparison between the simulated and observed meridional profiles of the mean zonal velocity u at 15 m depth using the independent observations from the Global Drifter Program climatology of Laurindo et al. (2017) (Fig. A4a), which strongly suggests the differences between the simulated and observed SEC velocities reflect gcm deficiencies.

A3. Mean zonal divergence

The simulated zonal divergence $\partial_x u$ (Figs. A3b,d,f and Fig. A4b) is less frequently evaluated in numerical simulations and less well constrained by observations but important to consider in this study of upwelling. The zonal divergence in both the simulation and observational products is estimated by the slope of a linear fit to the zonal velocities at each available depth and latitude (as in Johnson et al. 2001). We find that the simulated zonal divergence has a qualitatively similar spatial structure as all three observational estimates, although the observational patterns seem to have a somewhat larger amplitude and slightly different details. The most prominent feature of the zonal divergence is a tilted vertical dipole structure on the equator associated with the shoaling of the EUC from west to east and the associated convergence between 100 m and 250 m and divergence above 100 m. This dipole pattern is tilted in the depth-latitude plane such that the divergence above peaks south of the equator, while the convergence below peaks north of the equator (Figs. A3b,d,f and Fig. A4b). In the upper 50 m, there are also weaker convergences on both sides of the main divergence that are associated with the SEC, but the magnitude and size of these convergences varies substantially between observational products. There is another notable convergence at about 100 m below the NECC from 6-7°N. Finally, there is a notable divergence below the surface at about 150 m at 5°S between the bottom southern flank of the SEC and the SSCC.

Despite the qualitative similarities between our estimates of $\partial_x u$, there are considerable quantitative differences between the various estimates, especially in the top 30 m where the direct observations are only from drifters (Fig. A4b). Thus, even regionally integrated estimates of zonal divergence above 50 m, such as those in Fig. 2, remain significantly uncertain. Regional integrals over deeper depths where TAO data are available, e.g. between 50-200 m, are more consistent across observational products and thus seem more robust.

A4. Mean meridional velocity

Compared to the hydrography and zonal velocity, the meridional velocity is more challenging to quantify in observations and thus evaluate in our simulation. Perhaps the most robust spatially resolved observational estimate of the climatological meridional velocity can be obtained by combining all available satellite-tracked surface drifter observations from the global drifter program. These measurements have already been compiled into a gridded 1/4°-resolution monthly clima-

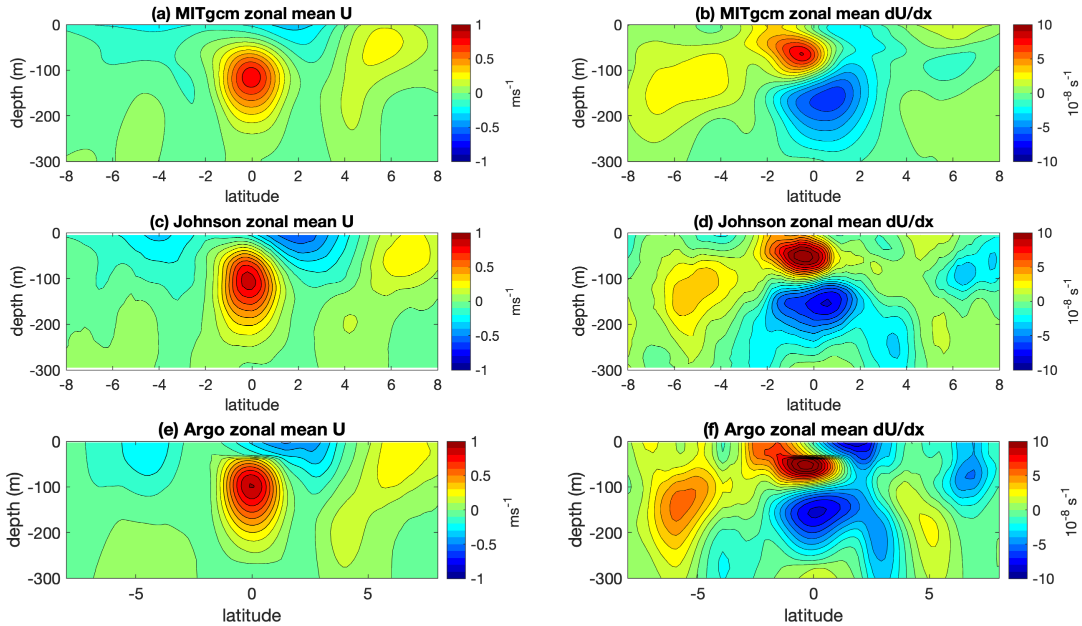

FIG. A3. The zonal mean zonal velocity u [(a), (c), (e)] and zonal divergence $\partial_x u$ [(b), (d), (f)] in the MITgcm (top), the Johnson et al. (2002) climatology of shipboard ADCP observations (middle), and the geostrophic zonal velocity derived from the 1/6° Argo climatology of Roemmich and Gilson (2009) (bottom).

tology by Laurindo et al. (2017). However, in the equatorial Pacific, the density of drifters is low enough and the currents are variable enough that the given uncertainty ranges from 5 to 10 cm/s, which is comparable in magnitude to the mean meridional velocity. To obtain a more precise estimate of this mean we take two additional averages. First, we average annually. Second, we average zonally over the longitudes where simulation output is available (97°W - 168°W). Uncertainties are derived from the standard errors on the zonal means, and the effective degrees of freedom are based on the empirical zonal autocorrelation of the residuals from a quadratic fit in longitude for each 1/4° of latitude and range in number from 15 to 30 (implying dominant autocorrelation scales of 3-8° longitude in the residuals). The resulting standard errors range from about 0.1-0.8 cm/s, which are an order of magnitude smaller than the means.

The comparison between the observed and simulated meridional profiles of meridional velocity at 15 m depth in Figure A5 suggest that the simulation is qualitatively realistic, but there are also some notable differences between the simulation and observations. Regarding the similarities,

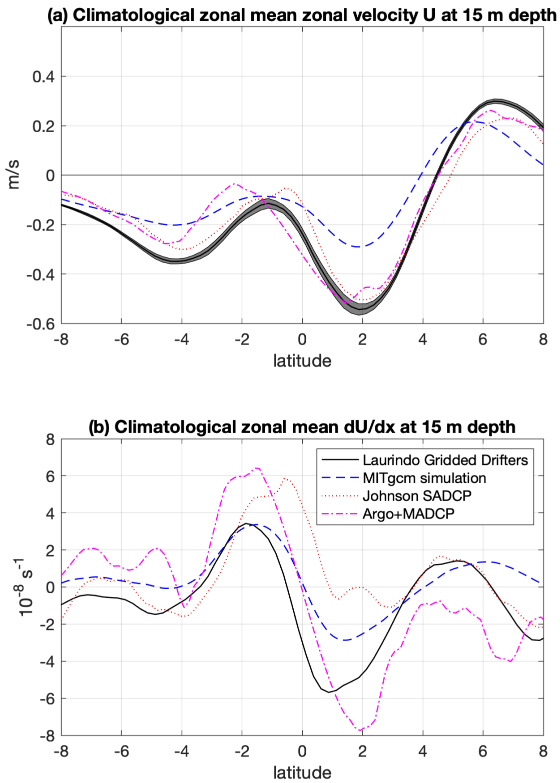

FIG. A4. The zonal mean zonal velocity u at 15 m depth (a) and zonal divergence $\partial_x u$ (b) at 15 m depth from the MITgcm simulation and three observational estimates: the gridded drifter observations of Laurindo et al. (2017), the Johnson et al. (2002) climatology of gridded shipboard ADCP observations, and the geostrophic zonal velocity derived from the 1/6° Argo climatology of Roemmich and Gilson (2009).

the observations and simulation both reveal a distinct peak in poleward flow between 1° and 4° from the equator. The peak is somewhat narrower or more prominent (but not necessarily greater in magnitude) on the northern than southern flank, where it spans a somewhat broader range of latitudes. In addition, the zero crossing occurs just north of but less than 1° from the equator such that the flow is southward on the equator with a speed of 2-4 cm/s. Finally, in both the simulation and observations, the poleward flow exhibits a qualitatively similar decay with latitude and meridional convergence poleward of about 3.5° on both flanks of the equator and reaches a speed near 4 cm/s at 8° from the equator, which is about half the peak speeds at lower latitudes. There is also a notable difference between the simulated and observed meridional velocity at 15 m:

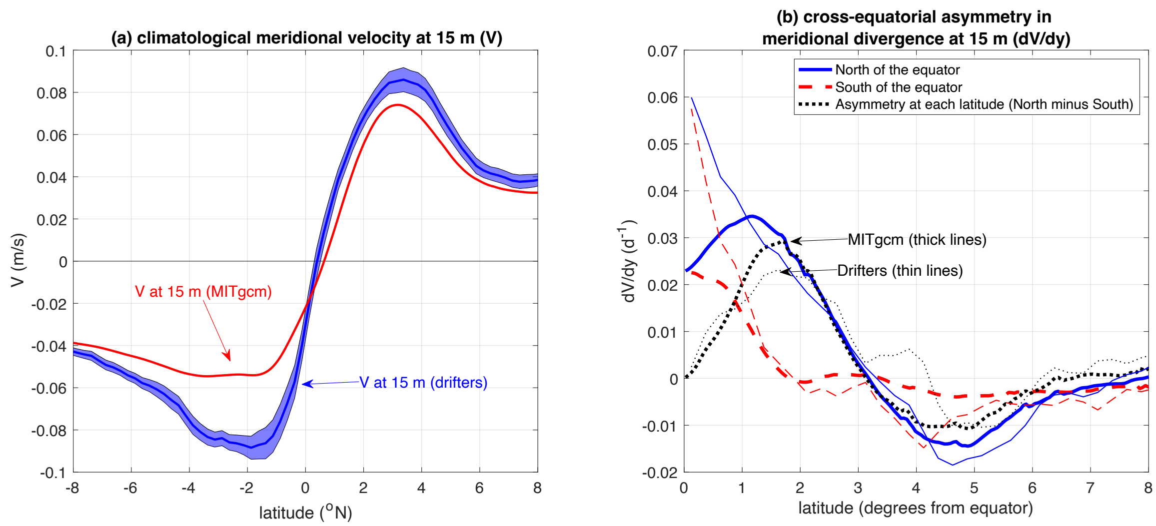

Fig. A5. The observed and simulated zonal and time mean meridional velocity v at 15 m depth (a) and meridional divergence $\partial_y v$ (b). In (a) the data are plotted as a function of latitude from 8°S to 8°N, whereas in (b) the data are plotted as a function of degrees from the equator to highlight the meridional asymmetries. In both panels, the observations are derived from the gridded climatology of meridional velocity based on the global satellite-tracked Lagrangian surface drifter program (Laurindo et al. 2017). The shading around the observational mean in (a) reflects ±1 standard error on the zonal mean at each latitude, where the effective degrees of freedom are calculated from the zonal autocorrelation of the residuals from a quadratic fit in longitude. In (b), the black lines show the meridional asymmetry, i.e. the difference, in meridional divergence at each latitude (northern hemisphere minus the southern hemisphere).

the meridional velocity is weaker in the model than in the observations, most notably the southern hemisphere peak that is only 5-6 cm/s in the simulation but 8-9 cm/s in the observations. It seems unlikely that such a large discrepancy is due to sampling or observational uncertainties and likely reflects a model deficiency, perhaps too-strong vertical mixing of momentum (see section 2c).

It is more difficult to evaluate the representation of the simulated meridional velocities at deeper depths, because we are less confident in the available observations. Although the geostrophic velocities are not well defined within about 3° of the equator (Fig. 9a), geostrophic equatorward meridional velocities are shown to be realistic but slightly weak using the zonal dynamic height gradients in Fig. A2. In addition, Fig. 2 shows indirectly that the meridional transports at 5°S and 5°N are fairly realistic by comparing the simulated and observed geostrophic and Ekman

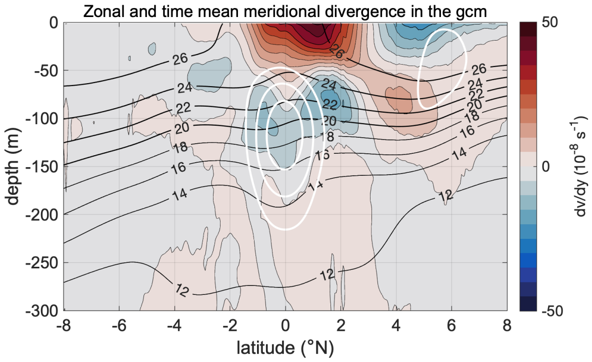

Fig. A6. The simulated time and zonal mean meridional divergence in the MITgcm. The meridional velocity is shown in Fig. 9c. For reference, potential temperature contours are overlaid in black and labeled, and zonal velocity contours are overlaid in white increasing from 0.2 m/s in 0.2 m/s increments.

transports at those latitudes. However, there is also one published direct observational estimate of the meridional velocity climatology that extends across all latitudes and depths of interest: the shipboard ADCP composite of Johnson et al. (2001), which represents a zonal and time mean during the 1990s over essentially the same longitudes as our model domain. The results are published in their Fig 5a, which we can compare with the analogous simulation results in our Figs. 9c. Qualitatively, the simulated and observed meridional velocity exhibit similar spatial patterns below the surface, i.e. the equatorward flow of the tropical cells at about 100 m depth, although there are some differences in detail that are mostly within the range of the fairly large 1-4 cm/s observational uncertainties. Perhaps the most robust quantitative difference is that the simulated meridional velocity at 15 m depth is somewhat weaker than observed, consistent with the drifter-based evaluation.

A5. Mean meridional divergence

The meridional divergence in the upper ocean is the dominant cause of equatorial upwelling and thus an especially important feature of the simulations to evaluate. Indirect and regionally-integrated estimates of the meridional divergence based on the geostrophic and Ekman transport across 5° are shown to be fairly realistic in Fig. 2. But direct and spatially-resolved evaluations of the simulated meridional divergence are especially valuable in this study of the finescale spatial structure in upwelling.

The strongest observational evidence in favor of the hypothesized meridional asymmetry in upwelling is the observation that the meridional divergence at 15 m has a similar cross-equatorial meridional asymmetry as the simulated meridional divergence, which in turn is closely related to the simulated meridional asymmetry in upwelling at 50 m. Specifically, differentiating the mean meridional velocity v at 15 m from the drifter observations (Fig. A5b) yields an estimate $\partial_y v$ with a very similar meridional structure and asymmetry as the simulation. There is considerable meridional asymmetry: roughly 3/4 of the divergence occurs north of the equator between 0° and 3°N versus 1/4 between 0° and 1°S. As a function of distance from the equator, the cross-equatorial difference in $\partial_y v$ at each latitude (i.e., 'asymmetry') is locally maximum between 1.5° and 2° from the equator (Fig. A5b). Here, $\partial_y v \approx 0.02 - 0.03$ d^{-1} on the north side of the equator but near zero on the south side. On the other hand, the observed meridional divergence is considerably stronger than the simulated meridional divergence equatorward of 1° and peaks at magnitudes about twice as strong. It may also be noted that the peak meridional divergence on the equator is still much less than the peak equatorial divergence estimated within 10 km of the equator by averaging the raw drifter tracks in long thin zonal slices (Poulain 1993; Karnauskas 2025). The estimate based on the drifter-based gridded velocities of Laurindo et al. (2017) is consistent with the maximally averaged estimate of Poulain (1993) with a 160 km meridional averaging scale. Nevertheless, the observed and simulated meridional divergence between 1° and 6° from the equator are quite similar and distinctly asymmetric across the equator (Fig. A5b) supporting the notion that the simulations capture the key physics of the asymmetric meridional divergence.

There is also considerable meridional asymmetry in the meridional divergence below 15 m depth, which has several lobes between 50 m and 150 m depth (Fig. A6; c.f. Fig. 6b in Johnson et al. (2001)). The observations and simulations exhibit a qualitatively similar pattern. From north to south, these lobes include a convergence at 5-6°N, a double peaked convergence spanning the EUC that is stronger and extends further from the equator on the northern flank, and finally a convergence at 3°S that is stronger in the observations than the simulations. Although there is considerable uncertainty in the observational estimate of the mean meridional divergence below 15 m, and the observations are from a different time period than the simulation, the good qualitative pattern comparison again suggests that both the observations and the simulation express the climatology to a first approximation, and the numerical simulation captures the key physics of the meridional circulation and divergence not only at 15 m but throughout the upper 200 m as well.

A6. Seasonal Cycle

A comparison of the observed and simulated seasonal cycles of SST as well as zonal and meridional velocity at 15 m depth were also conducted. The seasonal cycle of SST has been studied extensively and is quite realistic but not the focus of this study, so the comparisons are not shown. The seasonal cycle of the zonal velocity is also well studied and quite realistic as shown in Fig. A7, despite the deficiencies in the time mean (Fig. A3). However, the seasonal cycle of meridional velocity yields a somewhat less compelling comparison (Fig. A7). North of the equator, e.g. between 5-8°N, both the drifter observations and simulation have a robust and similar seasonal cycle in meridional velocity of order 0.1 m/s from peak (December-February) to trough (August-October). Unfortunately, observational uncertainty in the the monthly meridional velocity reaches 2-3 cm/s near the equator, which is comparable to or larger than the small seasonal variations there. And, the seasonal variability of 1-2 cm/s from peak to trough is also too weak from 5-8°S to yield clear patterns south of the equator, although the observational uncertainty drops to 1 cm/s.

A7. Variance

Several measures of the simulated variance are plotted and evaluated in comparson with observations in Figs. A8, A9, and A10. First, the daily mean sea-surface height (SSH) variance is calculated in each grid cell and zonally averaged in Fig. A8. The result is compared with an analogous calculation from the Copernicus/DUACS 1/4° resolution gridded sea-surface height anomalies from multimission altimetry (Taburet et al. 2019). Despite the fact that the real resolution of the altimetry product is really only about 800 km wavelength and several weeks in time, the variance is still double that of the MITgcm (Ballarotta et al. 2019). Much of the shorter variability is presumably due to internal waves generated by tides, which are thus missing from the MITgcm. But, still, the MITgcm has a SSH standard deviation that is up to 50% smaller.

Consistent with reduced variance in SSH, the upper ocean eddy kinetic energy from daily mean horizontal velocities is also lower in the MITgcm compared to observations from the ADCP data

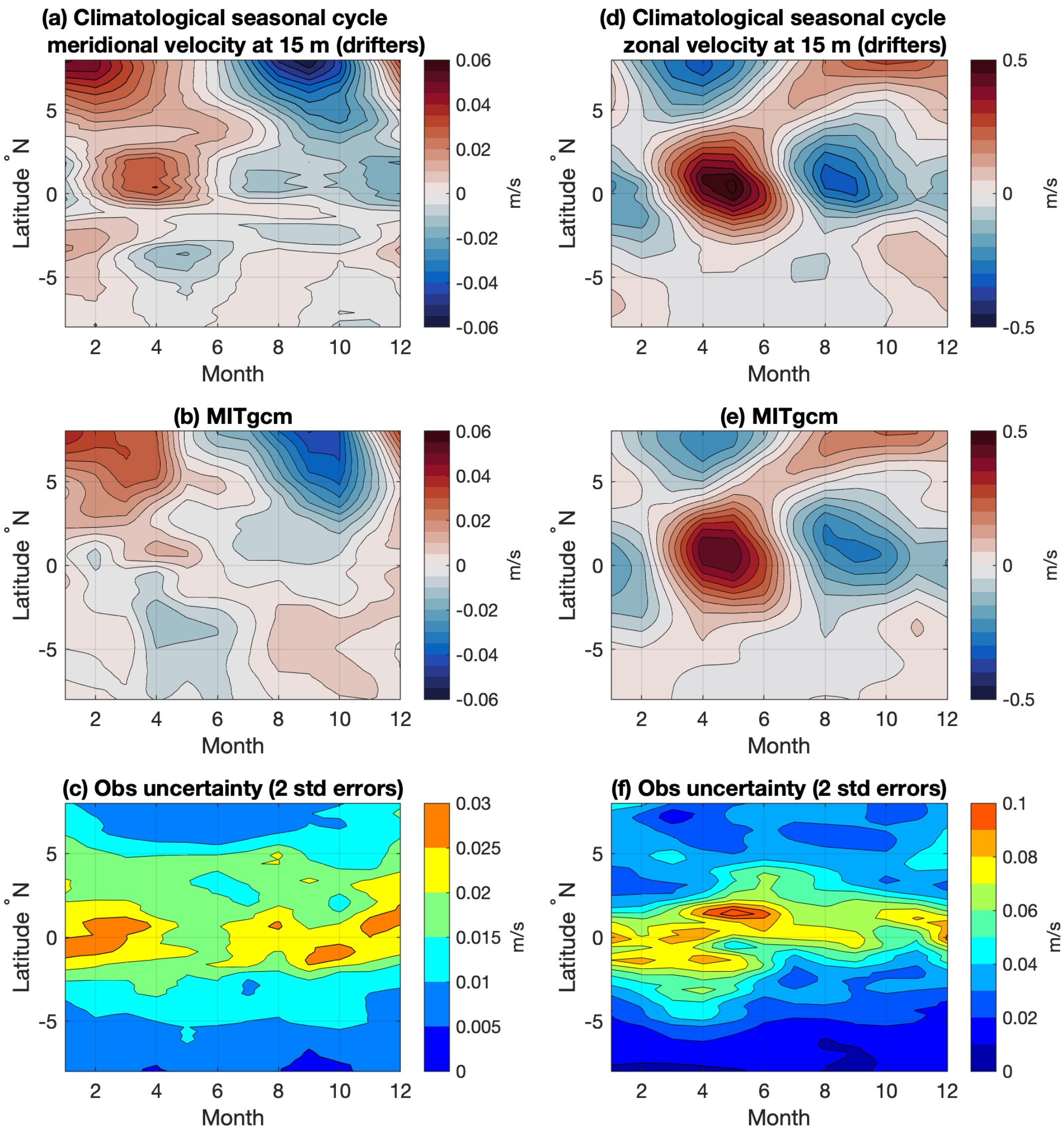

FIG. A7. The simulated 1999-2018 and zonal mean seasonal cycle of the meridional velocity (a) and zonal velocity (b) at 15 m (with annual means subtracted). The observational uncertainties are two standard errors on the zonal means, in which the degrees of freedom account for the zonal autocorrelation at each latitude.

collected on the TAO mooring at 0°,140°W (Fig. A9a-b) (McPhaden et al. 2010). In addition, the mooring data seems to exhibit stronger covariance between zonal and meridional velocity uv than in the simulation, although the depth structures are similar (Fig. A9c). For reference, we plot the

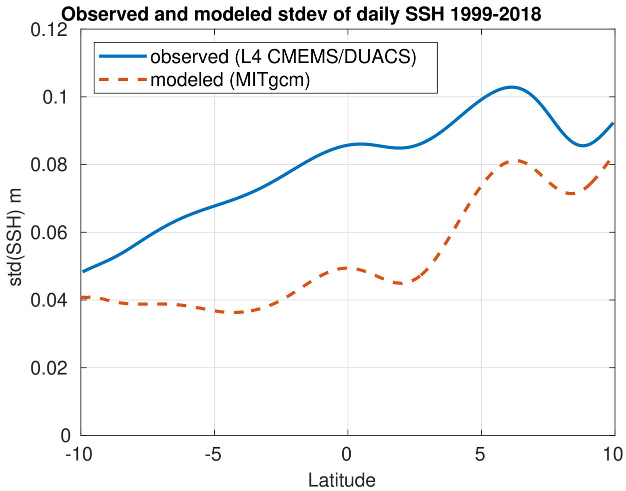

FIG. A8. The 1999-2018 and zonal mean standard deviation of daily sea surface height in the simulation and the AVISO/DUACS level 4 gridded multi-mission altimetry dataset from Copernicus Marine Services.

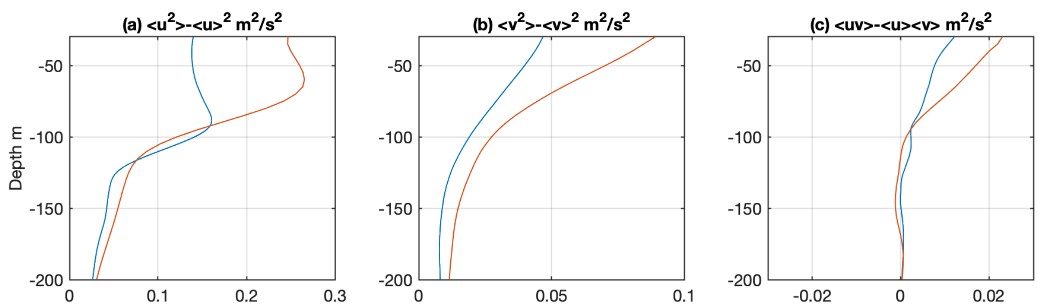

FIG. A9. The simulated (blue; MITgcm) and observed (red; TAO mooring) 1999-2018 time mean eddy (co)variances at 0°,140°W of the daily mean horizontal velocity: $\langle u^2\rangle - \langle u\rangle^2$ (a), $\langle v^2\rangle - \langle v\rangle^2$ (b), and $\langle uv\rangle - \langle u\rangle\langle v\rangle$ (c). Here, the angle brackets denotes a time mean.

meridional structure of the simulated climatological seasonal cycles of eddy (co)variances at 15 m depth in Fig. A10.

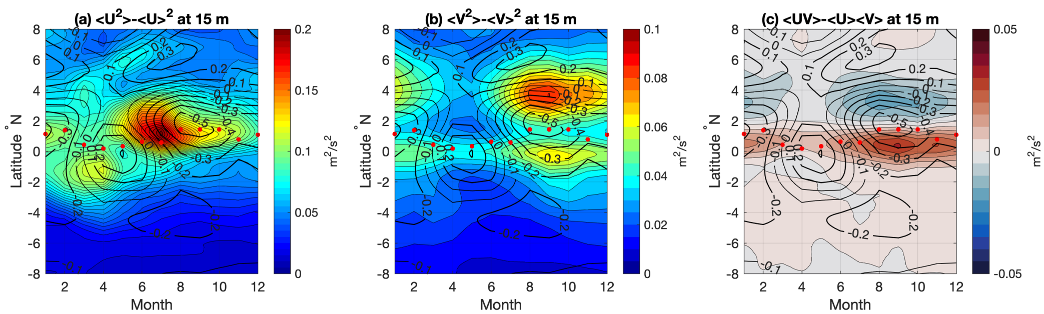

FIG. A10. The simulated 1999-2018 and zonal mean seasonal cycle of the horizontal velocity (co)variances at 15 m: zonal eddy kinetic energy $\langle u^2\rangle - \langle u\rangle^2$ (a), meridional kinetic energy $\langle v^2\rangle - \langle v\rangle^2$ (b), and the meridional flux of zonal velocity $\langle uv\rangle - \langle u\rangle\langle v\rangle$ (c). In this figure, the average denoted by angle brackets denotes a 1999-2018 monthly climatological and zonal mean. The red line marks the latitude where the maximum upwelling is achieved (see Fig. 4b) and black contours mark the climatological zonal velocity u.

References

Adcroft, A., C. Hill, J.-M. Campin, J. Marshall, and P. Heimbach, 2004: Overview of the formulation and numerics of the mit gcm. *Proceedings of the ECMWF seminar series on Numerical Methods, Recent developments in numerical methods for atmosphere and ocean modelling*, 139–149.

Ballarotta, M., and Coauthors, 2019: On the resolutions of ocean altimetry maps. *Ocean science*, **15 (4)**, 1091–1109.

Bjerknes, J., 1966: A possible response of the atmospheric hadley circulation to equatorial anomalies of ocean temperature. *Tellus*, **18 (4)**, 820–829.

Bonjean, F., and G. S. Lagerloef, 2002: Diagnostic model and analysis of the surface currents in the tropical pacific ocean. *Journal of Physical Oceanography*, **32 (10)**, 2938–2954.

Bryden, H. L., and E. C. Brady, 1985: Diagnostic model of the three-dimensional circulation in the upper equatorial pacific ocean. *Journal of Physical Oceanography*, **15 (10)**, 1255–1273.

Bryden, H. L., and E. C. Brady, 1989: Eddy momentum and heat fluxes and their effects on the circulation of the equatorial pacific ocean. *Journal of Marine Research*, **47 (1)**, 55–79.

Chelton, D. B., F. J. Wentz, C. L. Gentemann, R. A. de Szoeke, and M. G. Schlax, 2000: Satellite microwave sst observations of transequatorial tropical instability waves. *Geophysical Research Letters*, **27 (9)**, 1239–1242.

Cherian, D., D. Whitt, R. Holmes, R.-C. Lien, S. Bachman, and W. Large, 2021: Off-equatorial deep-cycle turbulence forced by tropical instability waves in the equatorial pacific. *Journal of Physical Oceanography*, **51 (5)**, 1575–1593.

Cromwell, T., 1953: Circulation in a meridional plane in the central equatorial pacific. *J. Mar. Res.*, **12**, 196–213.

Cronin, M. F., N. A. Bond, C. W. Fairall, and R. A. Weller, 2006: Surface cloud forcing in the east pacific stratus deck/cold tongue/itcz complex. *Journal of climate*, **19 (3)**, 392–409.

Crowe, M. N., and J. R. Taylor, 2018: The evolution of a front in turbulent thermal wind balance. part 1. theory. *Journal of Fluid Mechanics*, **850**, 179–211.

Deppenmeier, A.-L., F. O. Bryan, W. S. Kessler, and L. Thompson, 2021: Modulation of cross-isothermal velocities with enso in the tropical pacific cold tongue. *Journal of Physical Oceanography*, **51 (5)**, 1559–1574.

Eliassen, A., 1951: Slow thermally or frictionally controlled meridional circulation in a circular vortex. *Astrophisica Norvegica, v. 5, p. 19*, **5**, 19.

Flierl, G. R., and R. P. Mied, 1985: Frictionally induced circulations and spin down of a warm-core ring. *Journal of Geophysical Research: Oceans*, **90 (C5)**, 8917–8927.

Garrett, C. J. R., and J. Loder, 1981: Dynamical aspects of shallow sea fronts. *Philosophical Transactions of the Royal Society of London. Series A, Mathematical and Physical Sciences*, **302 (1472)**, 563–581.

Gent, P. R., and J. C. Mcwilliams, 1990: Isopycnal mixing in ocean circulation models. *Journal of Physical Oceanography*, **20 (1)**, 150–155.

Giordani, H., and G. Caniaux, 2011: Diagnosing vertical motion in the equatorial atlantic. *Ocean Dynamics*, **61**, 1995–2018.

Giordani, H., L. Prieur, and G. Caniaux, 2006: Advanced insights into sources of vertical velocity in the ocean. *Ocean Dynamics*, **56**, 513–524.

Halpern, D., and H. P. Freitag, 1987: Vertical motion in the upper ocean of the equatorial eastern pacific. *Oceanologica Acta, Special Issue*.

Halpern, D., R. A. Knox, D. S. Luther, and S. G. H. Philander, 1989: Estimates of equatorial upwelling between 140 and 110 w during 1984. *Journal of Geophysical Research: Oceans*, **94 (C6)**, 8018–8020.

Hansen, D. V., and C. A. Paul, 1984: Genesis and effects of long waves in the equatorial pacific. *Journal of Geophysical Research: Oceans*, **89 (C6)**, 10 431–10 440.

Hazeleger, W., P. de Vries, and G. J. van Oldenborgh, 2001: Do tropical cells ventilate the indo-pacific equatorial thermocline? *Geophysical research letters*, **28 (9)**, 1763–1766.

Holmes, R. M., L. N. Thomas, L. Thompson, and D. Darr, 2014: Potential vorticity dynamics of tropical instability vortices. *Journal of Physical Oceanography*, **44 (3)**, 995–1011.

Hoskins, B., 1974: The role of potential vorticity in symmetric stability and instability. *Quarterly Journal of the Royal Meteorological Society*, **100 (425)**, 480–482.

Hoskins, B. J., 1982: The mathematical theory of frontogenesis. *Annual review of fluid mechanics*, **14 (1)**, 131–151.

Hoskins, B. J., I. Draghici, and H. Davies, 1978: A new look at the ω-equation. *Quarterly Journal of the Royal Meteorological Society*, **104 (439)**, 31–38.

Huang, B., and Coauthors, 2017: Extended reconstructed sea surface temperature, version 5 (ersstv5): upgrades, validations, and intercomparisons. *Journal of Climate*, **30 (20)**, 8179–8205.

Johnson, G. C., M. J. McPhaden, and E. Firing, 2001: Equatorial pacific ocean horizontal velocity, divergence, and upwelling. *Journal of Physical Oceanography*, **31 (3)**, 839–849.

Johnson, G. C., B. M. Sloyan, W. S. Kessler, and K. E. McTaggart, 2002: Direct measurements of upper ocean currents and water properties across the tropical pacific during the 1990s. *Progress in Oceanography*, **52 (1)**, 31–61.

Karnauskas, K. B., 2025: How fast is the mean upwelling in the equatorial pacific ocean? *Journal of Climate*.

Lagerloef, G. S., G. T. Mitchum, R. B. Lukas, and P. P. Niiler, 1999: Tropical pacific near-surface currents estimated from altimeter, wind, and drifter data. *Journal of Geophysical Research: Oceans*, **104 (C10)**, 23 313–23 326.

Large, W. G., J. C. McWilliams, and S. C. Doney, 1994: Oceanic vertical mixing: A review and a model with a nonlocal boundary layer parameterization. *Reviews of geophysics*, **32 (4)**, 363–403.

Laurindo, L. C., A. J. Mariano, and R. Lumpkin, 2017: An improved near-surface velocity climatology for the global ocean from drifter observations. *Deep Sea Research Part I: Oceanographic Research Papers*, **124**, 73–92.

Lellouche, J.-M., and Coauthors, 2021: The copernicus global 1/12 oceanic and sea ice glorys12 reanalysis. *Frontiers in Earth Science*, **9**, 698 876.

Liu, C., F. Wang, A. Köhl, X. Wang, C. Wang, and K. J. Richards, 2025: Subsurface ocean turbulent mixing enhances central pacific enso. *Nature Communications*, **16 (1)**, 2315.

Maillard, L., J. Boucharel, and L. Renault, 2022: Direct and rectified effects of tropical instability waves on the eastern tropical pacific mean state in a regional ocean model. *Journal of Physical Oceanography*, **52 (8)**, 1817–1834.

Marshall, J., A. Adcroft, C. Hill, L. Perelman, and C. Heisey, 1997: A finite-volume, incompressible navier stokes model for studies of the ocean on parallel computers. *Journal of Geophysical Research: Oceans*, **102 (C3)**, 5753–5766.

McDougall, T. J., 1987: Neutral surfaces. *Journal of Physical Oceanography*, **17 (11)**, 1950–1964.

McPhaden, M. J., M. F. Cronin, and D. C. McClurg, 2008: Meridional structure of the seasonally varying mixed layer temperature balance in the eastern tropical pacific. *Journal of climate*, **21 (13)**, 3240–3260.

McPhaden, M. J., S. E. Zebiak, and M. H. Glantz, 2006: Enso as an integrating concept in earth science. *science*, **314 (5806)**, 1740–1745.

McPhaden, M. J., and Coauthors, 2010: The global tropical moored buoy array. *Proceedings of OceanObs*, **9**, 668–682.

McWilliams, J. C., 2021: Oceanic frontogenesis. *Annual Review of Marine Science*, **13 (1)**, 227–253.

McWilliams, J. C., and G. Danabasoglu, 2002: Eulerian and eddy-induced meridional overturning circulations in the tropics. *Journal of physical oceanography*, **32 (7)**, 2054–2071.

Meinen, C. S., and M. J. McPhaden, 2001: Interannual variability in warm water volume transports in the equatorial pacific during 1993–99. *Journal of physical oceanography*, **31 (5)**, 1324–1345.

Meinen, C. S., M. J. McPhaden, and G. C. Johnson, 2001: Vertical velocities and transports in the equatorial pacific during 1993–99. *Journal of Physical Oceanography*, **31 (11)**, 3230–3248.

Mitchell, T. P., and J. M. Wallace, 1992: The annual cycle in equatorial convection and sea surface temperature. *Journal of Climate*, **5 (10)**, 1140–1156.

Moum, J. N., A. Perlin, J. D. Nash, and M. J. McPhaden, 2013: Seasonal sea surface cooling in the equatorial pacific cold tongue controlled by ocean mixing. *Nature*, **500 (7460)**, 64–67.

Niiler, P. P., 1969: On the ekman divergence in an oceanic jet. *Journal of Geophysical Research*, **74 (28)**, 7048–7052.

Perez, R. C., M. F. Cronin, and W. S. Kessler, 2010: Tropical cells and a secondary circulation near the northern front of the equatorial pacific cold tongue. *Journal of physical oceanography*, **40 (9)**, 2091–2106.

Philander, S., and R. Pacanowski, 1981: The oceanic response to cross-equatorial winds (with application to coastal upwelling in low latitudes). *Tellus*, **33 (2)**, 201–210.

Poulain, P.-M., 1993: Estimates of horizontal divergence and vertical velocity in the equatorial pacific. *Journal of physical oceanography*, **23 (4)**, 601–607.

Proehl, J. A., 1998: The role of meridional flow asymmetry in the dynamics of tropical instability. *Journal of Geophysical Research: Oceans*, **103 (C11)**, 24 597–24 618.

Qiao, L., and R. H. Weisberg, 1997: The zonal momentum balance of the equatorial undercurrent in the central pacific. *Journal of Physical Oceanography*, **27 (6)**, 1094–1119.

Qiao, L., and R. H. Weisberg, 1998: Tropical instability wave energetics: Observations from the tropical instability wave experiment. *Journal of Physical Oceanography*, **28 (2)**, 345–360.

Quay, P., M. Stuiver, and W. Broecker, 1983: Upwelling rates for the equatorial pacific ocean derived from the bomb 14c distribution. *Journal of Marine Research*, **41**, 769–792.

Richards, K. J., S.-P. Xie, and T. Miyama, 2009: Vertical mixing in the ocean and its impact on the coupled ocean–atmosphere system in the eastern tropical pacific. *Journal of climate*, **22 (13)**, 3703–3719.

Risien, C. M., and D. B. Chelton, 2008: A global climatology of surface wind and wind stress fields from eight years of quikscat scatterometer data. *Journal of Physical Oceanography*, **38 (11)**, 2379–2413.

Roemmich, D., and J. Gilson, 2009: The 2004–2008 mean and annual cycle of temperature, salinity, and steric height in the global ocean from the argo program. *Progress in oceanography*, **82 (2)**, 81–100.

Shapiro, L. J., and H. E. Willoughby, 1982: The response of balanced hurricanes to local sources of heat and momentum. *Journal of Atmospheric Sciences*, **39 (2)**, 378–394.

Taburet, G., A. Sanchez-Roman, M. Ballarotta, M.-I. Pujol, J.-F. Legeais, F. Fournier, Y. Faugere, and G. Dibarboure, 2019: Duacs dt2018: 25 years of reprocessed sea level altimetry products. *Ocean Science*, **15 (5)**, 1207–1224.

Thomas, L. N., C. M. Lee, and Y. Yoshikawa, 2010: The subpolar front of the japan/east sea. part ii: Inverse method for determining the frontal vertical circulation. *Journal of physical oceanography*, **40 (1)**, 3–25.

Thomas, L. N., A. Tandon, and A. Mahadevan, 2008: *Submesoscale Processes and Dynamics*, 17–38. American Geophysical Union (AGU), https://doi.org/https://doi.org/10.1029/177GM04, URL https://agupubs.onlinelibrary.wiley.com/doi/abs/10.1029/177GM04.

Thompson, L., 2000: Ekman layers and two-dimensional frontogenesis in the upper ocean. *Journal of Geophysical Research: Oceans*, **105 (C3)**, 6437–6451.

Tsujino, H., and Coauthors, 2018: Jra-55 based surface dataset for driving ocean–sea-ice models (jra55-do). *Ocean Modelling*, **130**, 79–139.

Wang, S., and Coauthors, 2022: El niño/southern oscillation inhibited by submesoscale ocean eddies. *Nature Geoscience*, **15 (2)**, 112–117.

Weisberg, R. H., and L. Qiao, 2000: Equatorial upwelling in the central pacific estimated from moored velocity profilers. *Journal of Physical Oceanography*, **30 (1)**, 105–124.

Whitt, D., D. Cherian, R. Holmes, S. Bachman, R.-C. Lien, W. Large, and J. Moum, 2022: Simulation and scaling of the turbulent vertical heat transport and deep-cycle turbulence across the equatorial pacific cold tongue. *Journal of Physical Oceanography*, **52 (5)**, 981–1014.

Whitt, D., J. R. Taylor, and M. Lévy, 2017: Synoptic-to-planetary scale wind variability enhances phytoplankton biomass at ocean fronts. *Journal of Geophysical Research: Oceans*, **122 (6)**, 4602–4633.

Whitt, D. B., and L. N. Thomas, 2013: Near-inertial waves in strongly baroclinic currents. *Journal of Physical Oceanography*, **43 (4)**, 706–725.

Wyrtki, K., 1981: An estimate of equatorial upwelling in the pacific. *Journal of Physical Oceanography*, **11 (9)**, 1205–1214.

Yu, Z., J. P. McCreary Jr, and J. A. Proehl, 1995: Meridional asymmetry and energetics of tropical instability waves. *Journal of Physical Oceanography*, **25 (12)**, 2997–3007.